Applied Catalysis B: Environmental 321 (2023) 122045

Contents lists available at ScienceDirect

Applied Catalysis B: Environmental

journal homepage: www.elsevier.com/locate/apcatb

Ca doping effect on the performance of $La_{1-x}Ca_xNiO_3/CeO_2$-derived dual function materials for CO2 capture and hydrogenation to methane

Jon A. Onrubia-Calvo, A. Bermejo-López, B. Pereda-Ayo, José A. González-Marcos, Juan R. González-Velasco *

Department of Chemical Engineering, Faculty of Science and Technology, University of the Basque Country UPV/EHU, Campus de Leioa, Barrio Sarriena, ES-48940 Leioa, Bizkaia, Spain

ARTICLE INFO

Keywords:
Integrated CO_2 capture and utilization
CO_2 methanation
Dual function material
Perovskite
Ca doping
CeO_2 support

ABSTRACT

CO_2 valorization in form of synthetic natural gas is a convenient way to store large amounts of intermittent energy produced from renewable sources for long periods of time. Here reported research addresses the development of novel dual function materials (DFMs) for the utilization of CO_2 from simulated post-combustion effluent by cyclic adsorption and in-situ methanation. These DFMs, obtained after the controlled reduction of 20% $La_{1-x}Ca_xNiO_3/CeO_2$-type precursors (with x = 0–0.5), are widely characterized before and after catalytic tests. XRD diffractograms, H_2-TPD experiments and STEM-EDS images denote that Ca-doping shows low influence on materials composition, slight detrimental effect on textural properties and no influence on Ni, La and Ce distribution. Meanwhile, the concentration of Ca-based species increases as long as La^{3+} substitution by Ca^{2+} increases, which leads to a progressively promotion of medium and, especially, strong basic sites concentration (CO_2-TPD). As a result, the 20% $La_{0.5}Ca_{0.5}NiO_3/CeO_2$-derived DFM almost doubles (188.8 μmol g^{-1}) the CH_4 production of the 20% $LaNiO_3/CeO_2$-derived DFM (96.5 μmol g^{-1}) at high temperatures. Indeed, this novel DFM enhances the methanation capacity of the conventional 15% Ni-15% CaO/Al_2O_3 DFM (143.0 μmol CH_4 g^{-1}), with higher stability during long-term experiments and adaptability under variable feed compositions, which further support the applicability of these novel DFMs. Thus, Ca doping emerges as an effective way of tailoring CO_2 adsorption and in-situ hydrogenation to CH_4 efficiency of 20% $LaNiO_3/CeO_2$-derived DFMs.

1. Introduction

Carbon dioxide is the main cause of global warming and its presence in the atmosphere is increasing at the highest rate never observed (2.0 ppm/year) [1,2]. To reverse this situation, the International Energy Agency (IEA) considers the decarbonization of electric and thermal generation as main priority sectors, since they are responsible of two fifths of worlds CO_2 emissions. In Europe, decarbonization of the energy system is based on a massive implementation of renewable energies, which has reduced CO_2 emissions by 12% since 2009. However, moving in this direction implies having an energy mix with high percentages of intermittent energy, which can cause electrical surpluses increasing the complexity of the system to operate [3,4].

Nowadays, the electrical power obtained from wind turbines and solar panels can be stored in form of energy vector such as H_2 or CH_4. Hydrogen has a higher calorific value than methane (33.900 vs. 13.249 kcal kg^{-1}) and no CO_2 is formed during H_2 combustion. However, compared to methane it presents significantly lower density, making its storage considerably more expensive, and its large-scale transport infeasible due to incompatibility of the current gas grid. Hence, the conversion of renewable energy into methane (Power-to-Methane technology, PtM) seems to be currently a more suitable technology, not only because of the use of renewable energy but also because CO_2 anthropogenic emissions are reduced [5]. CO_2 methanation, also known as the Sabatier reaction (Eq. 1), is an exothermic process that can be used to valorize CO_2, in form of methane or synthetic natural gas (SNG), with H_2 preferably generated with surplus electric power from renewable energies [6]:

$$CO_2 + 4H_2 \rightleftarrows CH_4 + 2H_2O \quad \Delta H^0 = -164 \text{ kJ mol}^{-1} \tag{1}$$

As the reduction of the eight electrons of the CO_2 to CH_4 with hydrogen at low temperatures, is quite limited, this reaction is generally accelerated through the use of different catalytic formulations.

* Corresponding author.
E-mail address: juanra.gonzalezvelasco@ehu.es (J.R. González-Velasco).

https://doi.org/10.1016/j.apcatb.2022.122045
Received 23 July 2022; Received in revised form 30 September 2022; Accepted 3 October 2022
Available online 4 October 2022

However, this process usually needs a previous stage of CO_2 capture and sequestration (CCS), making its applicability challenging by technical-, energy- and cost-related issues [7,8]. Recently, a smart solution integrating CO_2 capture and utilization in a single reactor has been developed under the name of Dual Functional Materials (DFMs) [9,10]. The envisioned application of these materials is to cyclically capture CO_2 from combustion flue gas and to hydrogenate the captured CO_2 to produce CH_4 while regenerating the adsorbent. Thus, DFMs require the presence of a storage material to selectively adsorb CO_2 as well as an active site to activate adsorbed CO_2 hydrogenation. Alkaline or alkaline earth metals (such as Na, Ca or K) are typically used as CO_2 storage materials [9,11–15], whereas noble metals (such as Ru, Rh or Pt) [15–19] have been proposed to catalyze the methanation reaction. Both phases are usually dispersed on a high surface area carrier (such as Al_2O_3, SiO_2 or CeO_2) with the aim of increasing methane production rate [20].

Ru, with loadings in the range 1–5 wt%, is typically used as active site to carry out CO_2 methanation due to its high reducibility and activity [11,16,21,22]. However, its use increase drastically the cost of the DFM. Alternatively, Ni-based catalysts have been widely implemented for PtM technology, since they present the best cost to activity ratio. Nevertheless, their use as DFMs for combustion flue gas applications is hindered due to: their deactivation at low temperature as a result of a high interaction of nickel particles with CO, their poor reducibility at the temperatures at which methanation reaction is thermodynamically favourable (< 350 °C) and their heterogeneous particle size distribution [23,24]. Largely based on the pioneering research of Daihatsu and Toyota [25], the ex-solution of active metal NPs from a perovskite host, such as $LaNiO_3$, has been identified as a simple way to achieve a homogeneous active sites distribution, with good reversibility and controlled interactions of Ni sites with the support for the different formulations applied in the CO_2 methanation reaction [26–29].

For the first time in the literature, we explored in a recent study the use of $LaNiO_3$/support-type formulations (with support = CeO_2, Al_2O_3 and La-Al_2O_3) as precursor of dual function materials with highly dispersed Ni nanoparticles (NPs) in strong interaction with the rest of the components of the catalyst (Ce and La). Our results demonstrated that these novel formulations displayed high activity at low temperature and stability during CO_2 adsorption and in-situ hydrogenation cycles [30]. However, these DFMs showed a limited CH_4 production at higher temperatures, in comparison with conventional Ni-based formulations (such as Ni-Na_2CO_3/Al_2O_3 or Ni-CaO/Al_2O_3) [12]. Interestingly, it is well-known that the physicochemical properties of ABO_3-type perovskites, and as a consequence of their corresponding DFMs, can be easily regulated by the substitution of A- and B-site cations by other elements such as Ba, K, Na or Ca and Ru, Fe, Co and Mn, respectively. Based on our previous studies, focused on NO_x storage and reduction technology [31–33], the partial substitution of La^{3+} by other cations, such as Sr^{2+}, Ca^{2+}, Ba^{2+}, Mg^{2+}, K^+ or Ce^{4+}, emerges as an easy way of tuning surface basicity and, as a consequence, improving CO_2 adsorption and in-situ hydrogenation to methane. Among them, Ca^{2+} presents a similar ionic radius (1.34 Å) to La^{3+} (1.36 Å$^+$) and it is the alkaline adsorbent that has demonstrated the further promotion of the CH_4 production at high temperature for conventional formulations [16,18]. Thus, we hypothesize that the partial substitution of La^{3+} by Ca^{2+} in perovskite-based formulations could enhance CO_2 adsorption and in-situ CO_2 methanation efficiency of these novel materials, especially at high temperature.

In fact, the present paper focuses on analyzing the effect of Ca doping on CO_2 adsorption and hydrogenation to CH_4 efficiency of DFMs obtained from 20% $LaNiO_3$/CeO_2 precursors, which to our knowledge has not been reported to date. For that, a series of novel 20% $La_{1-x}Ca_xNiO_3$/CeO_2 (with x = 0–0.5) formulations are synthesized, widely characterized and their catalytic activity and stability are evaluated in cycles of CO_2 capture and in-situ methanation.

2. Experimental

2.1. Perovskite catalyst preparation

Ceria-supported $La_{1-x}Ca_xNiO_3$ perovskites (with x = 0–0.5) were prepared by combining citric acid and wetness impregnation methods. Firstly, CeO_2 support was obtained by the direct calcination of Ce $(NO_3)_3 0.6\ H_2O$ precursor (*Acros Organics,* 99.5%) at 500 °C for 4 h in static air. Once ceria support was obtained, stoichiometric amounts of La $(NO_3)_2 0.6\ H_2O$ (*Fluka Analytical,* ≥ 99.0%), $Ca(NO_3)_2 0.4\ H_2O$ (*EMSURE ACS,* ≥ 99.0%) and $Ni(NO_3)_2 0.6\ H_2O$ (*Supelco*, 99.9%) were dissolved into distilled water under vigorous stirring. Then, citric acid ($C_6H_8O_7$, *Sigma Aldrich,* 99.5–100.5%) was added, as a complexing agent, with a citrate to nitrate molar ratio of 1.1, and the pH of the mixture was adjusted to 7 with an ammonia solution (28–30% as NH_3, *Acros Organics*). The obtained solution was impregnated over the CeO_2 support inside a *Buchi B-480* rotary evaporator (vacuum and 35 °C). Finally, the supported gel precursor obtained was dried at 120 °C for 12 h and, ultimately, calcined in a horizontal tube furnace at 600 °C for 4 h under a flow of 5% O_2/N_2 to get the desired ceria-supported perovskite. The following samples were synthesized (listed from low to high La substitutions by Ca): 20% $LaNiO_3/CeO_2$, 20% $La_{0.9}Ca_{0.1}NiO_3/CeO_2$, 20% $La_{0.8}Ca_{0.2}NiO_3/CeO_2$, 20% $La_{0.7}Ca_{0.3}NiO_3/CeO_2$, 20% $La_{0.6}Ca_{0.4}NiO_3/CeO_2$ and 20% $La_{0.5}Ca_{0.5}NiO_3/CeO_2$.

2.2. Catalysts characterization

Powder X-Ray Diffraction (XRD) patterns were collected in a *Philips PW1710* difractometer. For that, the samples were subjected to Cu K_α radiation in a continuous scan mode from 5° to 70° 2θ with 0.02° 2θ per second sampling interval. *PANalytical X`pert HighScore* and *Winplotr* specific softwares were used for data treatment.

High Angle Annular Dark Field (STEM-HAADF) images were obtained in a CETCOR Cs-probe-corrected Scanning Transmission Electron Microscopy microscope (ThermoFisher Scientific STEM, formerly FEI Titan3) operating at 300 kV and coupled with a HAADF detector (Fischione). The instrument had a normal field emission gun (Shottky emitter) equipped with a SuperTwin lens and a CCD camera. The samples were mixed with ethanol solvent and dropped onto a holey amorphous carbon film supported on a copper grid. In order to obtain spatially resolved elemental chemical analysis of the samples, the TEM apparatus was also equipped with an EDAX detector to carry out X-ray Energy Dispersive Spectroscopy (EDS) experiments. A 2k x 2k Ultrascan CCD camera (Gatan) was positioned before the filter for TEM imaging (energy resolution of 0.7 eV). The acquisition time for the analysis was 50 ms per spectrum and the used energy dispersion was 0.2 eV pixel^{-1}.

Textural properties were determined by N_2 adsorption-desorption analysis at the nitrogen boiling temperature (−196 °C), using a *Micromeritics TRISTAR II* equipment. Prior to the analysis, all samples were degassed under N_2 flow at 300 °C (10 h) to remove humidity or any impurities adsorbed at the surface.

La, Ca, Ni and Ce contents were quantitatively determined by Inductively Coupled Plasma Atomic Emission Spectroscopy, ICP–AES, using a *Q-ICP-MS XSeries II* model of Thermospectrometer. Prior to the analysis, the samples were digested at 120 °C with an acidic mixture HNO_3:HCl = 1:3 in a *MARS 5 194A07* microwave.

Surface basicity and Ni dispersion were evaluated by temperature Programmed Desorption of CO_2 (CO_2-TPD) and H_2 (H_2-TPD) experiments performed on *Micromeritics AutoChem II* equipment. The samples, around 0.15 g, were loaded in a quartz tube reactor and reduced at 550 °C in a 5% H_2/Ar (50 mL min^{-1}) for 2 h. After reduction, the samples were cooled down to 40 °C using pure He. During CO_2-TPD experiments, the pretreatment was followed by the adsorption of CO_2 (5% CO_2/He, 50 mL min^{-1}) up to sample saturation (60 min). Then, samples were heated from 40 °C to 900 °C with a temperature ramp of 10 °C min^{-1} in He (50 mL min^{-1}). The CO_2 desorption was

continuously monitored with a *Hiden Analitical HPR-20 EGA* mass spectrometer. On the other hand, pure H_2 flow (50 mL min^{-1}) was feed for 60 min during saturation step in the H_2-TPD experiments. Then, samples were exposed to He for 60 min to remove the physically adsorbed H_2 and were heated from 40 to 900°C with a temperature ramp of 10 °C min^{-1} in helium atmosphere (50 mL min^{-1}). In this case, the gas stream was directly analyzed by a TCD detector.

The Ni dispersion (D), specific surface area (S_{Ni}) and average size (d_{Ni}) were estimated according the following equations:

$$D\left(\%\right) = \frac{2 \times V_{ad} \times M \times SF}{m \times P \times V_m \times d_r} \times 100 \quad (2)$$

$$S_{Ni} = \frac{2 \times V_{ad} \times N_A \times \delta_{Ni}}{m \times V_m} \quad (3)$$

$$d_{Ni} = \frac{6 \times 10^3 \times MF}{\rho_{Ni} \times S_{Ni}} \quad (4)$$

Where V_{ad} (mL) represents the volume of chemisorbed H_2 obtained after the integration of H_2-TPD profile, M is the molecular weight of Ni (58.69 g mol^{-1}); SF means the stoichiometric factor between the Ni and H in the chemisorption (supposed as 1) and m means the catalyst mass used for TPD measurement; MF is the mass fraction of Ni in the catalyst and V_m is just the molar volume of H_2 (22.4 L mol^{-1}); d_r is the reduction degree of nickel based on H_2-TPR results (supposed as 100%) and N_A is the Avogadro constant (6.02 $\times 10^{23}$ mol^{-1}); δ_{Ni} and ρ_{Ni} represent the atomic cross-sectional area of Ni (0.0649 nm^2) and Ni density (8.902 g cm^{-3}), respectively.

The reducibility of the perovskite-based precursors was investigated by Temperature Programmed Reduction (H_2-TPR) experiments in *Micromeritics AutoChem II* equipment. The quartz tube reactor was loaded with 0.12 g of sample, which was pretreated with 5% O_2/He mixture at 500 °C and then cooled down to 35 °C. Afterwards, samples were heated from 35 to 950°C at 10 °C min^{-1} in a 5% H_2/Ar mixture with a flow rate of 30 mL min^{-1}. Water generated during the reduction was removed using a cold trap before the gas stream was analyzed by a TCD detector. Aiming to detect the formation or the decomposition of additional compounds the outlet stream was continuously monitored with a *Hiden Analitical HPR-20 EGA* mass spectrometer.

The range of temperatures at which the samples are capable of producing CH_4 is analyzed by Temperature Programmed Surface Reaction (TPSR) experiments in a quartz tube reactor placed in a horizontal furnace. Firstly, 0.3 g of catalyst was pretreated with 5% H_2/Ar mixture (700 mL min^{-1}) at 550 ºC for 2 h and then cooled down to 50 °C. Once the desired DFM was obtained, the catalyst was exposed to a gas stream composed of 25% CO_2/Ar for 30 min up to its saturation. This step was followed by a purge with Ar for 30 min. Finally, the catalyst was heated from 50 to 700 °C at 10 °C min^{-1} in a 5% H_2/Ar mixture with a flow rate of 700 mL min^{-1}. Different compounds (CO_2, CH_4, CO and H_2O) concentrations were continuously monitored by an online *MultiGas 2000 MKS FT-IR* analyzer.

2.3. Catalytic activity

Catalytic experiments during CO_2 adsorption and in-situ hydrogenation to CH_4 were carried out in a vertical stainless steel tubular reactor loaded with 1 g of different samples (d_p = 0.3–0.5 mm) at atmospheric pressure and in the 280–520 °C temperature range. A thermocouple was directly inserted into the catalyst bed to measure the actual pretreatment and reaction temperatures. Prior to the reaction, different perovskite-based formulations were reduced at 550 °C in 10% H_2/Ar mixture for 2 h in order to obtain the corresponding DFM. During the storage step, 10% CO_2/Ar was fed for 1 min, followed by a purge with Ar for 2 min to remove the weakly adsorbed CO_2 as well as to prevent CO_2 and H_2 streams mixing. Then, during the hydrogenation step, 10% H_2/Ar was fed for 2 min, followed by a purge step with Ar for 1 min before starting again the following storage step. The flow rate of each mixture was controlled by mass flow controllers to resulting in total gas flow of 1200 mL min^{-1} in all periods, which corresponds to a GHSV of 140,000 h^{-1}. CO_2, CH_4, CO and H_2O concentrations were continuously monitored with a *MultiGas 2000 MKS FT-IR* analyzer.

Different catalytic parameters were estimated from these concentration values. The CO_2 adsorption capacity during the storage step was calculated with Eq. 5. The amount that leaves the reactor was subtracted from the amount fed. To determine the amount of CO_2 fed, the stream from the feed system was led directly to the analyzer. This profile corresponds to the actual CO_2 input that was fed to the reactor

$$\text{stored}CO_2\left(\mu\text{mol g}^{-1}\right) = \frac{1}{W}\int_0^t \left[F^{in}_{CO_2}(t) - F^{out}_{CO_2}(t)\right] dt \quad (5)$$

where $F^{in}_{CO_2}$ and $F^{out}_{CO_2}$ are the molar CO_2 flow (mol h^{-1}) at the reactor inlet and outlet, respectively. Meanwhile, W is the corresponding sample mass to each formulation.

On the other hand, the CH_4 (Y_{CH_4}), CO (Y_{CO}) and H_2O (Y_{H_2O}) productions during the hydrogenation step were calculated with Eqs. 6–8, respectively. Definitive catalytic parameters were calculated as average values of three consecutive cycles.

$$Y_{CH_4}\left(\mu\text{mol g}^{-1}\right) = \frac{1}{W}\int_0^t F^{out}_{CH_4}(t)dt \quad (6)$$

$$Y_{CO}\left(\mu\text{mol g}^{-1}\right) = \frac{1}{W}\int_0^t F^{out}_{CO}(t)dt \quad (7)$$

$$Y_{H_2O}\left(\mu\text{mol g}^{-1}\right) = \frac{1}{W}\int_0^t F^{out}_{H_2O}(t)dt \quad (8)$$

where $F^{out}_{CH_4}$, F^{out}_{CO}, and $F^{out}_{H_2O}$ are the molar CH_4, CO and H_2O flow (mol h^{-1}) at the reactor outlet, respectively.

CH_4 selectivity (S_{CH_4}) is determined by relating the CH_4 and CO productions (Eq. 9) since they were the only two products that were detected:

$$S_{CH_4}(\%) = \frac{Y_{CH_4}}{Y_{CH_4} + Y_{CO}} \times 100 \quad (9)$$

Finally, the carbon balance (CB) check was carried out from the following expression:

$$CB(\%) = \left(\frac{Y_{CH_4} + Y_{CO}}{\text{stored } CO_2}\right) \times 100 \quad (10)$$

3. Results and discusion

3.1. Catalysts characterization

3.1.1. Phases identification and distribution

Fig. 1a includes XRD patterns of the fresh-supported perovskites ($La_{1-x}Ca_xNiO_3/CeO_2$), the bulk $LaNiO_3$ perovskite and the ceria support. Intense and narrow diffraction peaks (▲) can be observed for the bulk $LaNiO_3$ perovskite at 23.3, 32.9, 47.4 and 58.7° 2θ (PDF number: 00–034–1028). These reflections are characteristic of the rhombohedral highly crystalline $LaNiO_3$ phase. Furthermore, weak peaks, in form of impurities, can be identified, which are characteristic of: (•) the hexagonal $La_2O_2CO_3$ (25.8, 30.4, 42.5, 47.4 and 54.7° 2θ, PDF number: 00–037–0804), (*) hexagonal $La(OH)_3$ (15.7 ° 2θ, PDF number: 01–075–1900) (□) the cubic NiO (37.3, 43.3 and 62.9° 2θ, PDF number: 00–047–1049) and (Δ) the tetragonal La_2NiO_4 (31.4° 2θ, PDF number: 01–072–1241) phases, respectively. The presence of La- and Ni-based impurities suggests that no all Ni^{3+}/Ni^{2+} and La^{3+} are inserted within the $LaNiO_3$ structure during its conformation, as a consequence of the limited stability of this perovskite. On the other hand, the ceria support

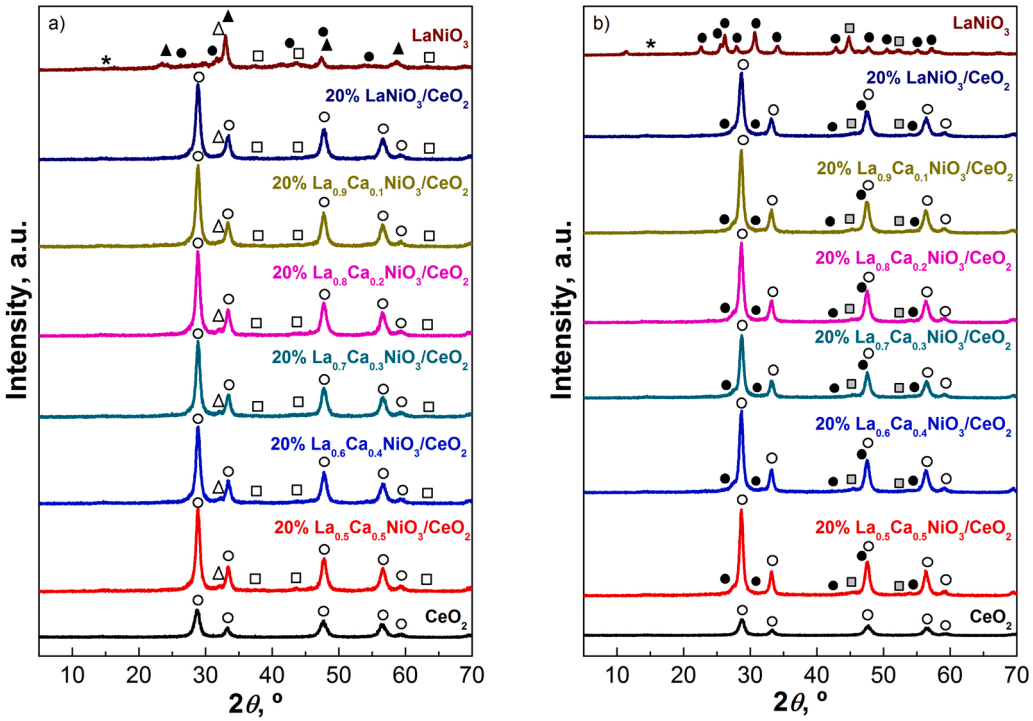

Fig. 1. XRD diffractograms of: a) fresh as well as b) reduced and used 20% $La_{1-x}Ca_xNiO_3/CeO_2$ samples, $LaNiO_3$ perovskite and CeO_2 support. (▲) represents $LaNiO_3$, (●) $La_2O_2CO_3$, (*) $La(OH)_3$, (□) NiO, (■) Ni^0, (Δ) La_2NiO_4 and (○) CeO_2.

shows intense and narrow diffraction peaks (○) at 28.6, 33.1, 47.5, 56.3 and 59.1° 2θ, which are characteristic of the highly crystalline ceria with cubic structure (PDF number: 00–034–0394). Supported samples show intermediate diffraction patterns between ceria support and bulk perovskite. As a result, the characteristic diffraction peaks of the CeO_2 and $LaNiO_3$ phases are overlapped, limiting their individual identification. However, the perovskite conformation can be confirmed by the presence of a weak peak at 23.3° 2θ (Fig. S1a), which is the only one not overlapped by those of the ceria support. Regarding to calcium doping effect, only a slight increase in the intensity of the characteristic diffraction peaks of $La_2O_2CO_3$, $La(OH)_3$, NiO and La_2NiO_4 phases is observed for high Ca contents (Fig. S1a). In agreement with our previous works [31–33], charge imbalance associated to calcium (Ca^{2+}) incorporation in the perovskite lattice in substitution of lanthanum (La^{3+}) could be compensated by alteration of the oxidation state of the transition metal (Ni^{4+} formation) or by the generation of oxygen vacancies in the lattice. Taking into account that nickel is expected to be accommodated in form of Ni^{3+}/Ni^{2+}, the later alternative seems to be more plausible. Thus, the increase of impurities formation for the highly doped perovskites is mainly ascribed to the lower structural stability derived from the partial substitution of the larger La^{3+} (ionic radius = 1.36 Å), by the smaller Ca^{2+} (ionic radius = 1.34 Å), as well as due to the negative charge defect derived from this substitution. In any case, the absence of CaO peaks as well as the similar diffraction patterns observed irrespectively of the Ca content, suggests that the crystalline structure of the $La_{1-x}Ca_xNiO_3$-type perovskites remains similar irrespectively La^{3+} substitution degree.

XRD measurements were also carried out for the different samples (Fig. 1b) after subjecting them to the reduction pretreatment (550 °C in 10% H_2/Ar mixture for 2 h) and the activity test. As can be observed, all ceria-supported samples maintain the intense and narrow diffraction peaks (○) identified for the fresh CeO_2 support, which confirms the high stability of this oxide. The intensity of these peaks (Fig. S1b) increases with respect to that observed for fresh samples (Fig. S1a), which suggests an increase of its crystallinity due to the treatment at high temperatures during reduction step as well as CO_2 methanation reaction. In contrast, no characteristic diffraction peaks are discernible for rhombohedral $LaNiO_3$ phase (▲), cubic NiO (□) and tetragonal La_2NiO_4 (Δ) phases. Meanwhile, the intensity of $La_2O_2CO_3$ (●) and $La(OH)_3$ (*) diffraction peaks increases. Furthermore, new diffraction peaks appear at 44.6 and 51.8 °2θ (■), which are characteristic of cubic Ni^0 phase (PDF number: 00–004–0850). As reported by Gallego et al. [34] and Bakiz et al. [35], the $La_2O_2CO_3$ phase is formed due to CO_2 adsorption on La_2O_3 sites, phase ex-solved during perovskite reduction pretreatment, whereas $La(OH)_3$ is formed due to the hydration of La_2O_3 phase with the H_2O formed during CO_2 methanation reaction [12,36]. Hence, XRD results confirm the complete reduction of $La_{1-x}Ca_xNiO_3$ perovskite, which leads to a controlled ex-solution of Ni^0 NPs as well as La_2O_3 formation. Finally, no additional diffraction peaks for Ca-based phases are identified at increasing Ca contents (Fig. S1b), which is assigned to the presence of CaO in nanodispersed state [37].

Metal contents were determined by ICP-AES analysis for the fresh samples. As can be observed, all metal contents are similar to nominal values (Table S1), which confirms the appropriate conformation of the perovskite phase irrespectively of calcium content. As expected, lanthanum content progressively decreases as long as calcium content increases.

Regarding to textural properties, Fig. S2 shows N_2-adsorption-desorption isotherms (−196 °C) for the fresh samples. All of them present a similar shape to IV-type isotherms, which are characteristic of mesoporous materials according to the IUPAC classification. Table 1 summarizes the textural parameters of the fresh and used 20% $La_{1-x}Ca_xNiO_3/CeO_2$ samples, which were determined from similar N_2-adsorption-desorption isotherms to that reported in Fig. S2. As can be observed, the specific surface areas (S_{BET}), progressively decrease for the fresh and used samples, as long as Ca content increases, whereas the pore volumes (V_p) and average pores size (d_p) increase. Specifically, the specific surface area drops from 34 $m^2\ g^{-1}$ for the used 20% $LaNiO_3/CeO_2$ sample to 29 $m^2\ g^{-1}$ for the 20% $La_{0.5}Ca_{0.5}NiO_3/CeO_2$ one, whereas the pore volume slightly increases from 0.12 $cm^3\ g^{-1}$ to 0.13 $cm^3\ g^{-1}$, and the average pore size from 101.9 Å to 126.9 Å. Taking into account these results, the slight decrease observed in the specific

Table 1
Specific surface areas (S_{BET}), pore volumes (V_p), average pore size (d_p), Ni^0 dispersion and Ni^0 average size for DFMs obtained from 20% $La_{1-x}Ca_xNiO_3/CeO_2$ (with x = 0–0.5) and $LaNiO_3$ precursors.

Sample	S_{BET}, m^2 g^{-1}	V_p, cm^3 g^{-1}	d_p, Å	D, %[a]	d_{Ni}, nm[b]
CeO_2	(78)[c]	(0.16)	(79.2)	–	–
20% $LaNiO_3/CeO_2$	34 (51)	0.12 (0.14)	122.9 (101.9)	25.8	3.9
20% $La_{0.9}Ca_{0.1}NiO_3/CeO_2$	30 (48)	0.12 (0.14)	135.5 (108.8)	23.5	4.3
20% $La_{0.8}Ca_{0.2}NiO_3/CeO_2$	30 (48)	0.12 (0.15)	144.8 (111.7)	22.2	4.6
20% $La_{0.7}Ca_{0.3}NiO_3/CeO_2$	31 (47)	0.13 (0.15)	142.3 (113.8)	23.2	4.4
20% $La_{0.6}Ca_{0.4}NiO_3/CeO_2$	31 (46)	0.13 (0.16)	149.1 (122.6)	22.7	4.5
20% $La_{0.5}Ca_{0.5}NiO_3/CeO_2$	29 (43)	0.13 (0.16)	152.9 (126.9)	22.9	4.4
$LaNiO_3$	12 (21)	0.09 (0.12)	155.2 (175.9)	7.5	13.4

[a] Ni^0 metal dispersion determined from H_2-TPD experiments.
[b] Ni^0 average size determined from H_2-TPD experiments.
[c] In brackets are shown the corresponding values to fresh samples, in relation to those obtained for used samples after reduction and CO_2 methanation reaction.

surface area is ascribed to the progressive overlap of small size pores, which ultimately is ascribed to the slight increase of the impurities concentration, previously identified by XRD analysis (Fig. 1).

In order to analyze the effect of Ca-doping on the morphology, particle size and different phases spatial distribution and aiming to confirm Ni^0 NPs, La_2O_3 and CaO conformation during the controlled ex-solution step, HAADF-STEM analysis were conducted. Fig. 2 includes STEM micrographs and the corresponding EDS elemental mapping of Ni, La, Ca and Ce for used 20% $LaNiO_3/CeO_2$, 20% $La_{0.8}Ca_{0.2}NiO_3/CeO_2$ and 20% $La_{0.6}Ca_{0.4}NiO_3/CeO_2$ DFMs. Furthermore, their Ni particle size distribution, estimated by measuring the size of, at least, 100 particles, is also included in the form of histogram. As can be observed, La (green color), Ca (orange color) and Ce (blue color) elements coexist with a homogeneous distribution in all analyzed areas. As expected, a noticeable increase in calcium concentration is observed for highly doped samples; however, it remains in nanodispersed state irrespectively of calcium content, in line with the absence of characteristic diffraction peaks for CaO phase in the XRD diffractograms (Fig. 1b). Regarding to Ni NPs (red color), homogeneously distributed spherical particles can be identified irrespectively of Ca content, which results in Ni^0 average particle sizes ranging between 5.6 and 5.9 nm in all cases, as observed on the right side histograms. Note that these values are in the range of those estimated from H_2-TPD experiments (Fig. S3), which are summarized in Table 2 (3.9–4.6 nm). Thus, DFMs with small-sized Ni NPs coexisting with homogeneously distributed La- and Ca-based phases over ceria support are obtained after subjecting the $La_{1-x}Ca_xNiO_3/CeO_2$-type formulations to controlled reduction step.

3.1.2. *Temperature programmed experiments (H_2-TPR and CO_2-TPD)*

It has been found that the reducing ability of La-based perovskites was strongly affected by the B site element properties [38]. H_2-TPR experiments provide information about the redox properties of the perovskites, which are mainly related to B site cation (Ni) nature. Special attention was paid on the identification of Ca doping effect on samples reducibility. Fig. 3 includes the H_2-TPR profiles, normalized per sample mass unit, of 20% $La_{1-x}Ca_xNiO_3/CeO_2$ samples, bulk $LaNiO_3$ perovskite and CeO_2 support.

Ceria support presents two main reduction peaks centered at 440 and 810 °C. The peak detected at lower temperature corresponds to the reduction of Ce^{4+} to Ce^{3+} at the surface; meanwhile, the reduction peak centered at 810 °C is ascribed to the incomplete reduction of the Ce^{4+} (Eq. 11) located into the bulk of ceria:

$$2CeO_2 + H_2 \rightarrow Ce_2O_3 + H_2O \quad (11)$$

The bulk $LaNiO_3$ perovskite shows a complex reduction profile, with

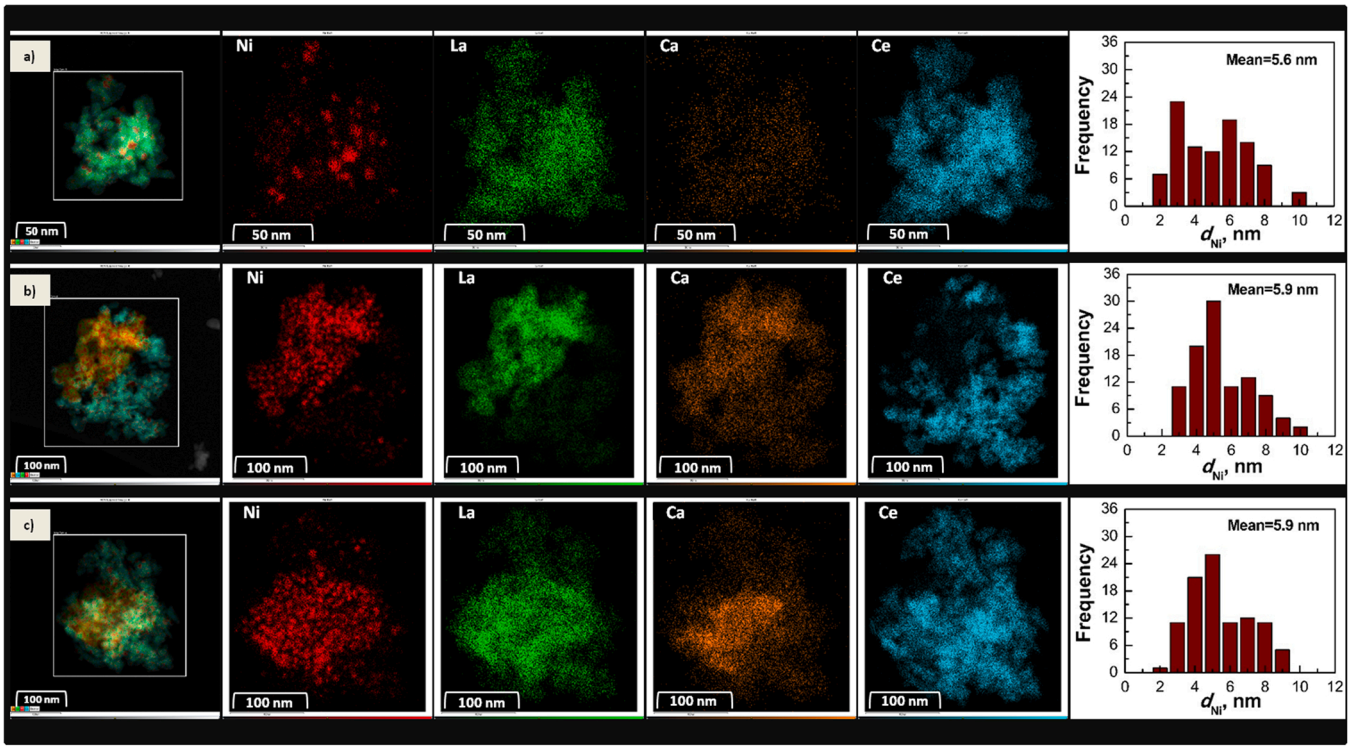

Fig. 2. STEM micrographs along with respective EDS elemental mapping of Ni, La, Ca and Ce for the DFMs obtained from: a) 20% $LaNiO_3/CeO_2$, b) 20% $La_{0.8}Ca_{0.2}NiO_3/CeO_2$ and c) 20% $La_{0.6}Ca_{0.4}NiO_3/CeO_2$ precursors. The Ni particle sizes distribution was also included for each sample in form of histogram.

Table 2
Deconvoluted H_2 consumption ascribed to the reduction of different species for 20% $La_{1-x}Ca_xNiO_3/CeO_2$ (with x = 0–0.5) formulations, bulk $LaNiO_3$ and CeO_2 support.

Sample	NiO + $LaNiO_3$ [a], μmol H_2 g^{-1}	$La_4Ni_3O_{10}$ + CeO_2 (surface) [b], μmol H_2 g^{-1}	La_2NiO_4 [c], μmol H_2 g^{-1}	CeO_2 (bulk) [d], μmol H_2 g^{-1}	Total [e], μmol H_2 g^{-1}
CeO_2	735.5	1310.1	264.2	4149.4	6459.2
20% $LaNiO_3/CeO_2$	865.6	2079.9	1010.2	2286.7	6242.4
20% $La_{0.9}Ca_{0.1}NiO_3/CeO_2$	823.9	2565.3	999.5	2397.3	6786.0
20% $La_{0.8}Ca_{0.2}NiO_3/CeO_2$	783.2	3372.5	997.9	2580.9	7734.4
20% $La_{0.7}Ca_{0.3}NiO_3/CeO_2$	729.3	3469.7	1003.7	3082.4	8285.1
20% $La_{0.6}Ca_{0.4}NiO_3/CeO_2$	662.8	3732.6	1205.5	3363.0	8964.0
20% $La_{0.5}Ca_{0.5}NiO_3/CeO_2$	638.3	4132.7	1232.9	3334.1	9338.1
$LaNiO_3$	1399.9	5873.5	3321.8	5310.7	15905.9

[a] Sum of integrated peaks located below 300 °C.
[b] Sum of integrated peaks located between 300 and 450 °C.
[c] Sum of integrated peaks located between 450 and 600 °C.
[d] Sum of integrated peaks located above 700 °C.
[e] Sum of all integrated peaks.

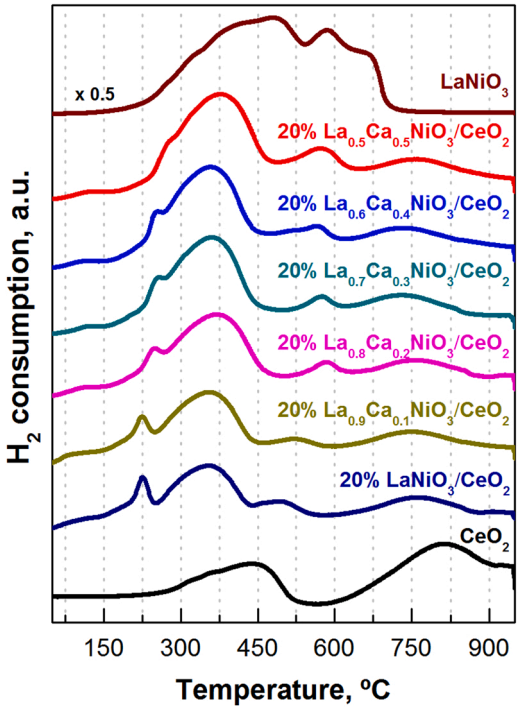

Fig. 3. H_2-TPR profiles normalized per sample mass unit of: 20% $La_{1-x}Ca_xNiO_3/CeO_2$ samples (with x = 0–0.5), bulk $LaNiO_3$ perovskite and CeO_2 support.

multiple contributions between 150 and 650 °C. As reported by Singh et al. [39], the $LaNiO_3$ perovskite reduction occurs following three consecutive steps:

$$4LaNiO_3 + 2H_2 \rightarrow La_4Ni_3O_{10} + Ni^0 + 2H_2O \quad (12)$$

$$La_4Ni_3O_{10} + 3H_2 \rightarrow La_2NiO_4 + 2Ni^0 + La_2O_3 + 2H_2O \quad (13)$$

$$La_2NiO_4 + H_2 \rightarrow 2Ni^0 + La_2O_3 + H_2O \quad (14)$$

The first step (Eq. 12) is as a consequence of the formation of $La_4Ni_3O_{10}$ phase due to the partial reduction of Ni^{3+}, within the $LaNiO_3$ perovskite to Ni^{2+} and corresponds to the peak centered around 330 °C. Furthermore, the NiO not accommodated in perovskite structure, which was previously identified by XRD analysis (Fig. 1a and S1a), can also be reduced within this temperature region. The second step is due to the complete reduction of Ni^{3+} to Ni^{2+} and corresponds to the peaks centered around 470 °C, leading to La_2NiO_4 formation (Eq. 13). Finally, the third reduction step (Eq. 14), peak centered around 590 °C, is associated with the reduction of Ni^{2+} of La_2NiO_4 formed at lower reduction temperatures (Eq. 13), and that already present in the sample (Fig. 1a). Once this reduction sequence is completed, Ni^0 and La_2O_3 are the only phases remaining in the sample in line with the observed by XRD analysis (Fig. 1b).

The reduction profiles of 20% $La_{1-x}Ca_xNiO_3/CeO_2$ samples are intermediate to that observed for the CeO_2 support and the bulk $LaNiO_3$ perovskite. As a consequence, two main H_2 consumption regions can be identified. The low temperature region (< 600 °C) consists on a broad reduction peak composed by three main contributions centered at 250, 355 and 560 °C. Based on for the reduction profile observed for bulk $LaNiO_3$ perovskite and CeO_2 support, these H_2 consumptions are ascribed to the progressive reduction of NiO, $LaNiO_3$ and La_2NiO_4 phases along with the surface reduction of the CeO_2 support. On the other hand, the peak centered at 750 °C is ascribed to the reduction of bulk CeO_2. Noteworthy, the reduction of different Ni-based species and ceria support occurs at significantly lower temperatures than in the reference bulk perovskite and ceria support. This fact denotes a remarkable enhancement of redox properties, which is ascribed to strong interaction between $LaNiO_3$ perovskite and ceria support, in line with the coexistence of different phases identified by STEM-EDS experiments (Fig. 2), aspect that promotes the H_2 spillover from Ni^0 sites to near ceria surface [40].

As long as Ca content increases, it can be noticed that the peaks ascribed to the partial reduction of Ni^{3+}, the NiO not accommodated in the perovskite structure (225–250 °C) and the ceria support (around 500–550 °C and 725–750 °C) tend to shift to higher temperatures. This fact is related to the progressive decrease of the specific surface area identified in Table 1 for the samples with increasing Ca contents. Furthermore, Ca doping also affects to different reducible species distribution, Table 2 shows the integrated area related to the reduction of the different species per gram of sample. As can be observed, the H_2 consumptions assigned to the reduction of different Ni-based phases as well as CeO_2 support progressively increase with the higher degree of substitution of lanthanum by calcium, except for the peak associated to the reduction of NiO and $LaNiO_3$ phases. As a result, the total H_2 consumption increases from 6424.4 μmol H_2 g^{-1}, for the 20% $LaNiO_3/CeO_2$ sample, to 9520.8 μmol H_2 g^{-1}, for the 20% $La_{0.5}Ca_{0.5}NiO_3/CeO_2$

sample. However, taking into account that Ni and CeO_2 are the only reducible species (Eqs. 11–14) and observing that similar contents are obtained for both phases (Table S1), no significant changes in H_2 consumption were expected. Thus, the increasing H_2 consumption observed should be related to an additional phenomenon.

In order to explain this increasing trend, H_2-TPR experiments were also followed by mass spectroscopy (Fig. S4). As can be observed, as long as Ca content becomes higher, two increasing CH_4 production peaks can be observed at 300 ºC and 500 ºC. Taking into account that the Sabatier reaction implies the consumption of 4 molecules of H_2 per 1 molecule of CO_2 (Eq. 1), the increasing H_2 consumption for higher Ca contents can be ascribed to the additional reaction of H_2 with adsorbed CO_2 to produce methane. Based on XRD experiments, it is assumed that most of the Ca^{2+} ions are inserted into the perovskite lattice, resulting in structural defects, mainly oxygen vacancies, which can adsorb CO_2, specie that can be converted into CH_4 at low temperatures during H_2-TPR experiments [41]. On the other hand, the increase in the CH_4 production at high temperatures is ascribed to a higher concentration of CO_2 adsorbed on catalysts surface. Note that this peak is almost negligible for the samples with low Ca contents ($x < 0.3$) and is followed by an increasing CO_2 desorption peak for high the samples with Ca contents. As a result of the simultaneous CH_4 production, the second (H_2 consumption between 250 and 450 °C) to first peak (H_2 consumption below 250 °C) ratio is between 2.4 and 6.5, which is higher than the theoretical value (1.5) expected from the stoichiometry of Eqs. 12 and 13.

The effect of Ca doping on CO_2 adsorption and activation is analyzed by performing CO_2-TPD experiments on 20% $La_{1-x}Ca_xNiO_3/CeO_2$ samples, which were pre-reduced following a similar procedure to that reported in catalytic experiments. In order to determine different basic sites nature, Fig. 4a shows CO_2 desorption profiles for the bare support (CeO_2), the bulk perovskite ($LaNiO_3$) and the 20% $La_{0.6}Ca_{0.4}NiO_3/CeO_2$ sample. Ceria support shows a single desorption peak, centered at 125 °C. This peak is assigned to the decomposition of weakly adsorbed species in form of bridged, hydrogen and bidentate carbonates on ceria surface [42]. In contrast, $LaNiO_3$ perovskite shows three main peaks at 100, 475 and 750 °C, respectively. The desorption peak observed at lowest temperature is ascribed to the decomposition of adsorbed CO_2 on Ni^0 NPs exsolved during samples pretreatment [43]. On the other hand, the desorption peaks at intermediate and high temperatures are assigned to the progressive decomposition of previously identified (Fig. 1) monodentate carbonates ($La_2O_3CO_3$) adsorbed on highly dispersed and bulk-like La_2O_3 species [28,44], respectively. Finally, the $La_{0.6}Ca_{0.4}NiO_3/CeO_2$ sample shows an intermediate CO_2-TPD profile to that described for bare support and bulk perovskite. However, a noticeable shoulder can be observed at higher temperatures of the peak centered at 100 °C. As reported in own previous study [29], this contribution is ascribed to the desorption of CO_2 from carbonates formed on Ni-CeO_2 interface as well as to an easier decomposition of CO_2 adsorbed on highly dispersed La_2O_3 sites due to its higher specific surface area (Table 1). Furthermore, a new desorption peak can be observed at 550 °C, which could be related to the additionally introduced basic sites due to the partial substitution of lanthanum by calcium. As observed by Philipp and Fujimoto [45], this process can be related to monodentate carbonates formation on Ca-sites ($CaCO_3$), which favor a more rapid adsorption of CO_2 on them than on La-sites [46].

Once the nature of different basic sites was identified, the effect of calcium doping on their distribution is analyzed. Fig. 4b shows the corresponding CO_2-TPD profiles of ceria-supported $LaNiO_3$ perovskites (20% $La_{1-x}Ca_xNiO_3/CeO_2$). According to the observed for the references samples, supported perovskites present three main desorption regions, which are classified as weak (50–200 °C), medium (250–625 °C) and strong (625–900 °C) basic sites. As expected, the desorption peaks centered at 550 °C as well as the contributions observed above this temperature tend to increase with higher calcium contents, which further validates the assignation made in Fig. 4a.

More specific information about the different species distribution was obtained after the deconvolution and integration of different desorption peaks. Table 3 summarizes weak, medium and strong basic

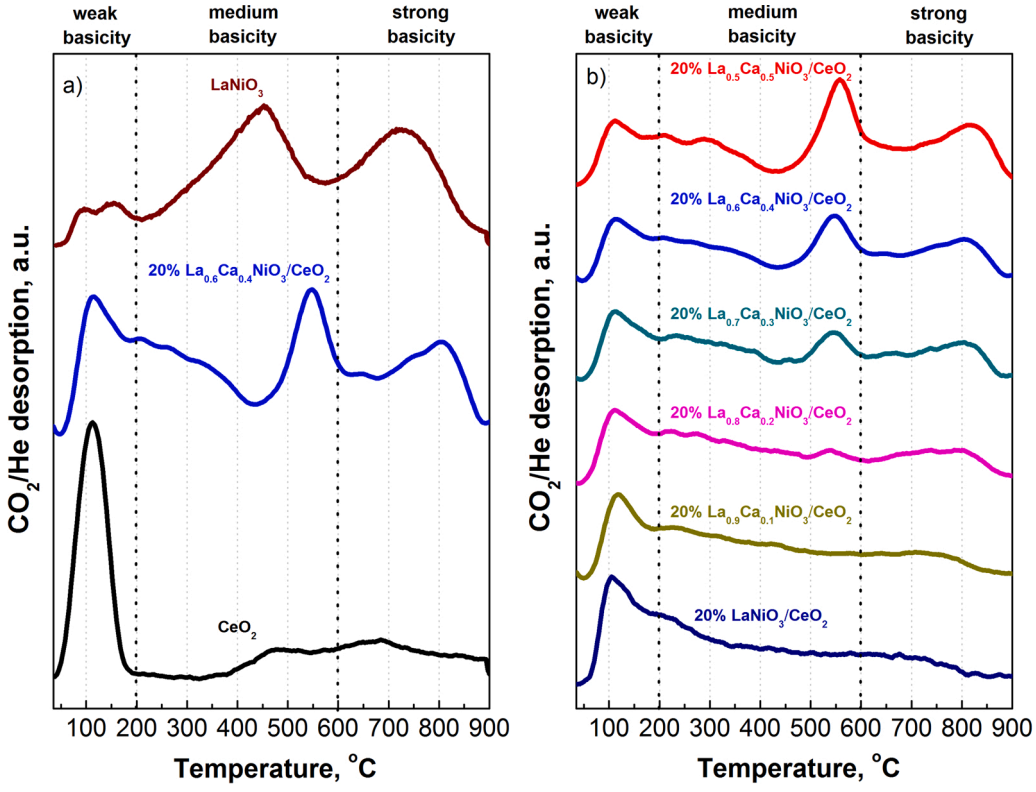

Fig. 4. CO_2-TPD profiles normalized per sample mass unit of pre-reduced: a) bulk $LaNiO_3$ perovskite, 20% $La_{0.6}Ca_{0.4}NiO_3/CeO_2$ sample and CeO_2 support, and b) 20% $La_{1-x}Ca_xNiO_3/CeO_2$ samples (with x = 0–0.5).

Table 3
Deconvoluted CO_2 desorption related to different basic sites, surface basic sites density and adsorbent utilization ratio for 20% $La_{1-x}Ca_xNiO_3/CeO_2$ (with x = 0–0.5) formulations, CeO_2 support and bulk $LaNiO_3$ sample.

Sample	Weak basicity[a], μmol CO_2 g-1	Medium basicity[b], μmol CO_2 g-1	Strong basicity[c], μmol CO_2 g-1	Medium + strong basic sites density[d], μmol$_2^{CO}$ m-2	Ratio CO_2/($CaO+La_2O_3$)[e]
CeO_2	49.6	8.0	26.3	0.4	–
20% $LaNiO_3/CeO_2$	31.5	104.5	32.6	4.0	0.24
20% $La_{0.9}Ca_{0.1}NiO_3/CeO_2$	26.9	104.5	37.2	4.7	0.24
20% $La_{0.8}Ca_{0.2}NiO_3/CeO_2$	24.1	106.0	42.8	5.0	0.25
20% $La_{0.7}Ca_{0.3}NiO_3/CeO_2$	21.9	102.9	49.6	4.9	0.25
20% $La_{0.6}Ca_{0.4}NiO_3/CeO_2$	19.1	100.9	55.4	5.0	0.25
20% $La_{0.5}Ca_{0.5}NiO_3/CeO_2$	18.5	123.6	85.8	7.2	0.36
LNO	11.6	75.0	73.3	12.4	0.07

[d]Sum of all integrated peaks.
[a] Sum of integrated peaks located below 200 °C.
[b] Sum of integrated peaks located between 200 and 600 °C.
[c] Sum of integrated peaks located above 600 °C.
[d] Determined as the μmoles of CO_2 desorbed between 200 and 550 °C per specific surface area.
[e] Moles of CO_2 desorbed per mol of ($CaO+La_2O_3$), once the amount desorbed from the ceria support was subtracted.

sites concentrations for all supported samples, ceria support and bulk perovskite. In general, the concentration of weak basic sites decreases, whereas the concentration of the medium and strong basic sites progressively increases as long as calcium content increases. Specifically, the concentration of weak, medium and strong basic sites ranges between 90.9 and 27.5, 64.3–157.9 and 9.4–68.9 μmol CO_2 $^{g-1}$ for the 20% $LaNiO_3/CeO_2$ and 20% $La_{0.5}Ca_{0.5}NiO_3/CeO_2$ samples, respectively. Taking into account that the ceria is the main weak basic site, the decrease of weakly adsorbed CO_2 species is ascribed to a lower accesibility of the ceria surface as a consequence of the pogressive decrease of specific surface (Table 1). On the other hand, the increasing medium and strong basic sites concentration is ascribed to a higher concentration and accesibility of Ca-based adsorption sites with respect to La-based ones. Note that no diffraction peaks were observed for CaO in Fig. 1 and a higher distribution degree of Ca-based phases with respecto to La-based ones can be deduced from the results reported in Fig. 2. In order to gain insigths on this aspect, Table 3 also includes the basic sites surface density of the sum of medium and strong basic sites. As observed, this parameter increases from 4.0 μmol $_2^{CO\ m\text{-}2}$ for 20% $LaNiO_3/CeO_2$ sample to 7.2 μmol $_2^{CO\ m\text{-}2}$ for the 20% $La_{0.5}Ca_{0.5}NiO_3/CeO_2$ one, which confirms that substituting La^{3+} by Ca^{2+} increases the concentration of medium-strong CO_2 adsorption sites. Furthermore, the accesibility of medium and strong basic sites is evaluated by determining the ratio of desorbed moles of CO_2 per mol of adsorbent (La_2O_3 and CaO). For the determination of this parameter, the amount of CO_2 desorbed from CeO_2 support was substracted in all cases. According to decomposition reactions of lanthanum and calcium carbonates, 1 mol of CO_2 should be desorbed per mol of La_2O_3 ($La_2O_2CO_3 \rightleftarrows La_2O_3 + CO_2$) and CaO ($CaCO_3 \rightleftarrows CaO + CO_2$). As observed, this ratio is below 1 irrespectively of sample composition. However, its value increases from 0.24 to 0.36, as long as Ca content in the sample becomes higher. These results evidence that Ca doping significantly enhances medium and strong basic sites concentration and accesibility.

3.1.3. Temperature programmed surface reaction (TPSR) of pre-adsorbed CO_2 with H_2

H_2-TPSR experiments were performed to evaluate the reducibility of CO_2 adsorbed species over the DFMs obtained after the controlled reduction of 20% $La_{1-x}Ca_xNiO_3/CeO_2$ (with x = 0–0.5) precursors (Fig. 5). Note that these experiments were performed by, first, conforming the corresponding DFM through the reduction of the sample at

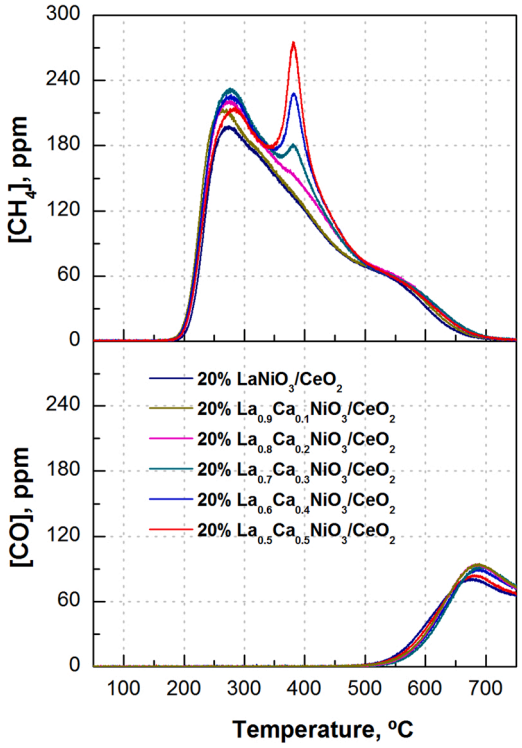

Fig. 5. CH_4 and CO formation during TPSR experiment of pre-adsorbed CO_2 with H_2 for the DFMs obtained after the controlled reduction of 20% $La_{1-x}Ca_xNiO_3/CeO_2$ (with x = 0–0.5) precursors.

550 °C (2 h), secondly, saturating the surface at 50 °C with CO_2, and finally, subjecting the sample to a 5% H_2/Ar mixture while the temperature is raised from 50 to 750 °C. A broad CH_4 formation peak (200–600 °C), centered around 275 °C, and with a long tail is observed for all analyzed catalysts. This peak is ascribed to the progressive methanation of CO_2 pre-adsorbed on basic sites of different nature, as deduced by CO_2-TPD experiments (Fig. 4). It is worth to mention that CH_4 formation is observed even above 500 °C, which highlights the great stability of the adsorbed carbonates. However, the CH_4 breakthrough

occurs at lower temperatures than in H_2-TPR (Fig. S4) experiment, whereas its formation is limited to a narrower temperature range than CO_2 decomposition observed in CO_2-TPD (Fig. 4) experiment. The former is ascribed to the presence of Ni^0 from the beginning of the TPSR experiment due to the pre-reduction step. Meanwhile, the later phenomena is related to the promotion of carbonates decomposition and reduction under net reducing environment, respectively.

Focusing on Ca doping effect, two different trends can be observed below and above 350 ºC. On the one hand, the main peak centered at 275 ºC tends to increase as long as Ca content increases up to La^{3+} substitution by Ca^{2+} of 30%. Above this Ca content, this peak progressively decreases and slightly shifts to higher temperatures. As observed in STEM-EDS images (Fig. 2), La_2O_3 is progressively substituted by nanodispersed CaO, which promotes a higher proximity between Ni^0 NPs and CO_2 storage component and, as a consequence, favors the decomposition and reduction of adsorbed CO_2 [16]. On the other hand, a new contribution, centered around 375 ºC, proggresively appears as long as Ca content increases. In agreement with the appearance of a increasing CO_2 desorption peak at 550 ºC for the formulations with La^{3+} substitution by Ca^{2+} above the 20% (Fig. 4) as well as with the increasing strong basic sites concentration, these results denote that Ca incorporation favors the formation of more stable carbonates under net reducing environment. Ultimately, these facts favor the CO_2 hydrogenation to CH_4 at higher temperatures. As a result, the samples showing more stable carbonates species also show the highest CH_4 production (Table 4) during H_2-TPSR experiment. Specifically, the CH_4 production increases from 130.3 μmol g^{-1} for the 20% $LaNiO_3/CeO_2$ to 159.6 μmol g^{-1} for the 20% $La_{0.5}Ca_{0.5}NiO_3/CeO_2$ sample. Finally, minor CO production is observed above 500 ºC irrespectively Ca content, which denotes high ability of the developed DFMs to carry out the complete CO_2 hydrogenation and discards the intermediacy of CO in the CO_2 methanation reaction.

3.2. Catalytic activity

3.2.1. CO_2 adsorption and hydrogenation to CH_4 mechanism onto 20% $La_{1-x}Ca_xNiO_3/CeO_2$ perovskites

Fig. 6 shows the concentration profiles of CO_2, CH_4, CO and H_2O at the reactor outlet for a complete CO_2 adsorption and methanation cycle at 480 ºC carried out with pre-reduced 20% $LaNiO_3/CeO_2$ and 20% $La_{0.5}Ca_{0.5}NiO_3/CeO_2$ samples, once the steady state has been reached. The CO_2 concentration profile when the reactor is bypassed is also included as reference. CO_2 adsorption and hydrogenation profiles are obtained by cyclically linking successive periods of CO_2 adsorption and hydrogenation with intermediate stages of purge with Ar to avoid CO_2 and H_2 mixing.

During the CO_2 adsorption period (1 min), a gas stream containing 1.6% CO_2 in Ar is fed to the reactor. As can be observed in Figs. 6a and 6b, the CO_2 concentration at the reactor outlet is almost negligible at the beginning of the storage step due to the complete adsorption of CO_2 on surface basic sites of both DFMs. As the adsorption period proceeds, CO_2 adsorption sites become saturated and CO_2 concentration at the outlet increases rapidly almost achieving the inlet concentration value at the end of this period.

Previously reported results [30] as well as what observed by CO_2-TPD (Fig. 4) and XRD experiments (Fig. S1) suggest that the CO_2 adsorption occurs preferentially onto La_2O_3 phase, in form of $La_2O_2CO_3$, and, in minor extent, on NiO-CeO_2 interface for the non-substituted sample (Fig. 6a). This process can be described by the following reaction:

$$La_2O_3 + CO_2 \rightleftarrows La_2O_2CO_3 \quad (15)$$

However, the slower saturation of CO_2 adsorption sites observed for Ca-doped sample (Fig. 6b) suggests the participation of different storage sites. In agreement with the observed by CO_2-TPD experiments (Fig. 4), the partial substitution of La^{3+} by Ca^{2+} provides additional basic sites, which enhances the CO_2 storage capacity. Based on the results reported in previous works [47,48], this process could occur in form of carbonates according to the following reactions:

$$CaO + CO_2 \rightleftarrows CaCO_3 \quad (16)$$

It is worth to mention that the storage process is accompanied by H_2O detection, revealing a displacement of pre-adsorbed H_2O by the progressive CO_2 adsorption on same basic sites [12,16]. This process can occur on $La(OH)_3$ sites (Eq. 17), previously identified by XRD analysis (Fig. S1) or, alternatively, on $Ca(OH)_2$ (Eq. 18) ones through the following reaction pathway:

$$2La(OH)_3 + CO_2 \rightleftarrows La_2O_2CO_3 + 3\ H_2O \quad (17)$$

$$Ca(OH)_2 + CO_2 \rightleftarrows CaCO_3 + H_2O \quad (18)$$

In agreement with this CO_2 adsorption mechanism, CO_2 signal start to be detectable after 15–20 s from the beginning of the adsorption period, achieving its maximum concentration at the end of this period. In contrast, H_2O desorption start to be detectable few seconds delayed and reach its maximum concentration after 50–60 s. Thus, CO_2 adsorption occurs preferentially onto free La_2O_3 and CaO sites (Eqs. 15 and 16) and; then, once those sites are occupied, the CO_2 adsorption occurs on previously hydrated $La(OH)_3$ and $Ca(OH)_2$ sites (Eqs. 17 and 18). Furthermore, a small CO signal is observed during adsorption period. The formation of this compound could be related to the incomplete hydrogenation of adsorbed CO_2 with H_2 chemisorbed on the Ni^0 sites formed during the previous hydrogenation step following the reverse water gas shift reaction (RWGS):

$$H_2 + CO_2 \rightleftarrows CO + H_2O \quad (19)$$

As expected, this process occurs immediately after CO_2 concentration start to increase. Then, when H_2O start to be released, CO production drops since in the presence of H_2O the equilibrium of the RWGS moves to the side reactants. At the same time, the simultaneous depletion of H_2 adsorbed on Ni^0 sites also contributes to limit RWGS reaction.

It is worth to mention that the formation of CO through the progressive decomposition of adsorbed formate species cannot be discarded ($HCOOH \rightarrow H_2O + CO$). This process is assisted with the H_2 chemisorbed on the previous hydrogenation step [49].

Once the adsorption period is completed, the sample and the reaction system are purged with a constant Ar flow rate to avoid gas mixing. As a consequence, CO_2 and H_2O signals progressively decrease reaching zero value during this period. The amount of CO_2 adsorbed onto the catalysts during the storage and following purge periods is determined by Eq. 5 and summarized in Table 5. As can be observed, 113 and 175 μmol CO_2 are adsorbed on the DFMs obtained from 20% $LaNiO_3/CeO_2$ and 20% $La_{0.5}Ca_{0.5}NiO_3/CeO_2$ precursors, respectively. Thus, these values demonstrate that CO_2 adsorption is promoted by partial substitution of La^{3+} by Ca^{2+}, in line with the observed by CO_2-TPD (Fig. 4) and TPSR (Fig. 5) experiments.

Finally, the hydrogenation period begins by the admission of 10% H_2/Ar gas mixture during 2 min. After the addition of H_2 in the gas stream, the stability of the carbonates is reduced and, as a consequence, their decomposition and subsequent conversion to CH_4 on Ni sites is

Table 4
CH_4 and CO formation during TPSR experiments of pre-adsorbed CO_2 with H_2 for 20% $La_{1-x}Ca_xNiO_3/CeO_2$ (with x = 0–0.5) formulations.

Sample	CH_4, μmol^{g-1}	CO, μmol^{g-1}
20% $LaNiO_3/CeO_2$	130.3	51.5
20% $La_{0.9}Ca_{0.1}NiO_3/CeO_2$	141.0	52.2
20% $La_{0.8}Ca_{0.2}NiO_3/CeO_2$	148.6	51.9
20% $La_{0.7}Ca_{0.3}NiO_3/CeO_2$	155.6	53.1
20% $La_{0.6}Ca_{0.4}NiO_3/CeO_2$	159.5	53.6
20% $La_{0.5}Ca_{0.5}NiO_3/CeO_2$	159.6	54.7

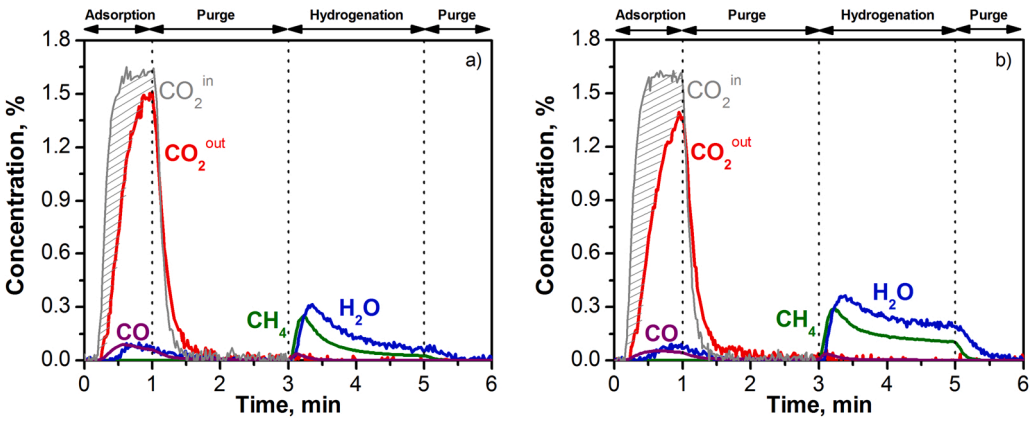

Fig. 6. CO_2, CH_4, H_2O and CO concentration profiles during one CO_2 adsorption and hydrogenation to CH_4 cycle at 480 ºC of DFMs obtained after the controlled reduction of: a) 20% $LaNiO_3/CeO_2$ and b) 20% $La_{0.5}Ca_{0.5}NiO_3/CeO_2$ precursors.

Table 5
CO_2 stored, CO produced, and released CO_2 and H_2O released during the adsorption step as well as CH_4, CO and H_2O produced during the hydrogenation step at 480 ºC for 20% $LaNiO_3/CeO_2$ and 20% $La_{0.5}Ca_{0.5}NiO_3/CeO_2$ samples.

	period	Adsorbed CO_2[a], μmol g^{-1}	CH_4[b], μmol g^{-1}	CO[c], μmol g^{-1}	H_2O[d], μmol g^{-}	CB[e], %	H_2O/CH_4 ratio[f]
20% $LaNiO_3/CeO_2$	Ads.	113.0	0.0	32.0	24.3	98.3	2.03
	Hyd.	–	74.6	4.5	128.2		
20% $La_{0.5}Ca_{0.5}NiO_3/CeO_2$	Ads.	175.0	0.0	24.2	24.3	97.4	2.03
	Hyd.	–	139.8	6.6	251.1		

[a] CO_2 adsorbed during the CO_2 adsorption and the following purge steps.
[b] CH_4 produced during hydrogenation and the following purge steps.
[c] CO produced during the adsorption or hydrogenation periods and the corresponding following purge steps.
[d] H_2O released during the adsorption or hydrogenation periods and the corresponding following purge steps.
[e] Carbon balance during a complete CO_2 adsorption and hydrogenation cycle.
[f] H_2O to CH_4 ratio during a complete CO_2 adsorption and hydrogenation cycle.

favored. As a result, an intense CH_4 peak with long tail that continues during the whole period is detected immediately after the beginning on the hydrogenation period, whereas H_2O formation is delayed around 10 s from CH_4 identification. The temporal evolution of CH_4 and H_2O can be described through the following reaction scheme:

$$\text{Step 1a: } La_2O_2CO_3 \rightleftarrows La_2O_3 + CO_2 \quad (20)$$

$$\text{Step 1b: } CaCO_3 \rightleftarrows CaO + CO_2 \quad (21)$$

$$\text{Step 2: } 4\ H_2 + CO_2 \rightleftarrows CH_4 + 2\ H_2O \quad (22)$$

$$\text{Step 3a: } La_2O_3 + 3\ H_2O \rightleftarrows 2La(OH)_3 \quad (23)$$

$$\text{Step 3a: } CaO + H_2O \rightleftarrows Ca(OH)_2 \quad (24)$$

$$\text{Step 3c: } Ce_2O_3 + 3\ H_2O \rightleftarrows 2Ce(OH)_3 \quad (25)$$

Firstly, lanthanum oxide carbonates as well as calcium carbonates are decomposed releasing CO_2 (Eqs. 20 and 21). Then, the CO_2 released reacts with hydrogen to form CH_4 and H_2O following Sabatier reaction (Eq. 1). Considering the stoichiometry of Eqs. 19, 2 molecules of H_2O should be detected per molecule of CH_4. In this sense, 74 μmol of CH_4 and 128.2 μmol of H_2O are produced for the 20% $LaNiO_3/CeO_2$-derived DFM, whereas these compounds production increases up to 139.8 μmol of CH_4 and 251.1 μmol of H_2O for the 20% $La_{0.5}Ca_{0.5}NiO_3/CeO_2$-derived DFM. As a result, the experimental H_2O/CH_4 ratios obtained during hydrogenation step are 1.73 and 1.79 for the DFMs obtained from 20% $LaNiO_3/CeO_2$ and 20% $La_{0.5}Ca_{0.5}NiO_3/CeO_2$ precursors, respectively. Taking into account that according to Eq. 1 a ratio of 2 is expected, this trend confirms that a fraction of H_2O is stored on La_2O_3 and CaO sites through the Eqs. 22 and 23. The participation of ceria on this process cannot be discarded (Eq. 24). In any case, the obtained values suggest that Ca doping prevents H_2O molecules adsorption in form of hydroxyls, since the 20% $La_{0.5}Ca_{0.5}NiO_3/CeO_2$-derived DFM shows an experimental ratio closer to 2 [46]. Thus, the higher CH_4 production observed for Ca-doped sample is related to the presence of a higher concentration and accessibility of CO_2 adsorption sites at the surface as well as to the limited competitive adsorption of H_2O with respect to non-doped sample. Ultimately, this fact results in a higher amount of CO_2 adsorbed during storage period (Table 5). Furthermore, an almost negligible CO signal (around 4.5–6.6 μmol CO g^{-1}), produced through RWGS reaction (Eq. 19), is observed during hydrogenation period.

If the entire CO_2 adsorption and hydrogenation to CH_4 cycle is considered, H_2O/CH_4 ratios increase up to 2.03 for both samples. This value is close to the stoichiometry ($H_2O/CH_4 = 2$) defined by Sabatier reaction (Eq. 1). Regarding to carbon balance, it is also adequately closed within ± 5%, since the quotient between the sum of CH_4 as well as CO produced during a complete CO_2 adsorption and hydrogenation cycle and the CO_2 stored during adsorption period is close to 1 for both samples (Table 5). These values support the validity of the obtained result and the proposed reaction scheme.

3.2.2. *Ca-doping effect on CO_2 adsorption and hydrogenation to CH_4 cycles*

Similar CO_2 adsorption and hydrogenation cycles have been performed between 280 and 520 ºC with the DFMs obtained after the reduction of 20% $La_{1-x}Ca_xNiO_3/CeO_2$ (with x = 0–0.5) formulations. With the aim of mimic a more realistic effluent gas the inlet CO_2 concentration has been increased from 1.6% to 10% throughout these experiments. From the obtained results, the amount of CH_4 and CO produced per cycle has been calculated according to Eqs. 6 and 7. Note that the carbon balance closes with an error below 5% for all experiments and the accuracy and the reproducibility of all experiments can be confirmed by the repetitive evolution of CO_2, CH_4 and H_2O obtained during consecutive CO_2 adsorption and hydrogenation cycles, as shows

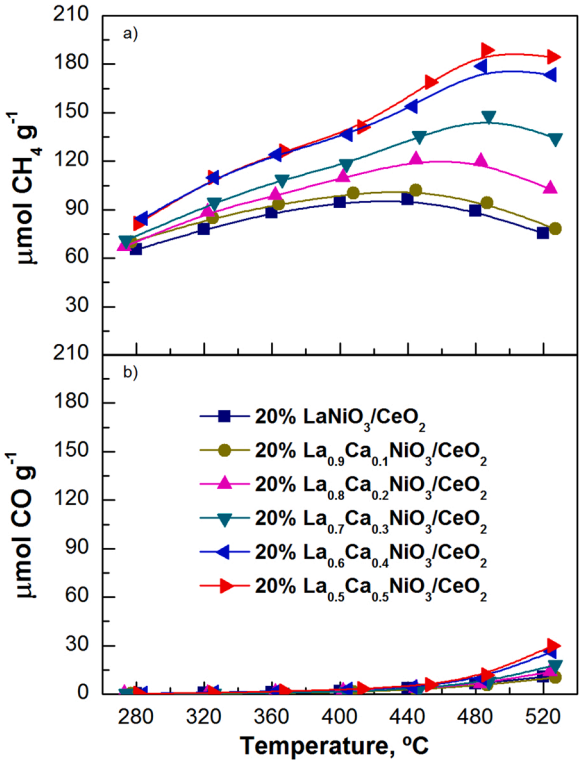

Fig. 7. Evolution of CH_4 and CO production with temperature for the DFMs obtained after the controlled reduction of 20% $La_{1-x}Ca_xNiO_3/CeO_2$ (with x = 0–0.5) precursors.

Fig. S5 for the 20% $La_{0.7}Ca_{0.3}NiO_3/CeO_2$-derived DFM.

Fig. 7 plots the evolution of CH_4 and CO production with temperature for all 20% $La_{1-x}Ca_xNiO_3/CeO_2$-derived DFMs. As can be observed in Fig. 7a, the CH_4 production is promoted in whole temperature range as long as Ca content increases, especially at high temperatures. Furthermore, increasing Ca contents shift the maximum CH_4 production to higher temperatures. Specifically, the highest CH_4 production is achieved at 400 and 480 ºC for the 20% $LaNiO_3/CeO_2$ and $La_{0.5}Ca_{0.5}NiO_3/CeO_2$ samples, respectively. Above these temperatures CH_4 production decreases while the reaction temperature increases due to a lower stability of adsorbed carbonates. Evaluating Ca doping effect, the maximum CH_4 production increases from 96.5 μmol CH_4 g^{-1} for the 20% $LaNiO_3/CeO_2$ sample (400 ºC) to 188.8 μmol CH_4 g^{-1} for the 20% $La_{0.5}Ca_{0.5}NiO_3/CeO_2$ one (400 ºC).

Regarding to CO production (Fig. 7b), this parameter increases continuously with the temperature due to the promotion of the RWGS reaction (Eq. 19) during the hydrogenation step. Furthermore, CO production also increases with higher Ca contents, which is ascribed to the enhanced CO_2 adsorption capacity. Nevertheless, its value is low compared to CH_4 production and almost negligible below 480 °C. These results denote a high selectivity towards CH_4 irrespectively the reaction temperature. Specifically, the selectivity towards CH_4 is above 94–95% below 520 ºC for all developed formulations.

To gain insight on the differences in CH_4 production, Fig. 8 shows CH_4 concentration profiles during a complete CO_2 adsorption and hydrogenation cycle for the DFMs obtained from 20% $LaNiO_3/CeO_2$, 20% $La_{0.8}Ca_{0.2}NiO_3/CeO_2$ and 20% $La_{0.6}Ca_{0.4}NiO_3/CeO_2$ precursors, respectively. As can be observed, the evolution of CH_4 signal is significantly affected by Ca content, especially at intermediates-high temperatures. On the one hand, similar CH_4 production profiles are observed at 280 (Fig. 8a) and 400 ºC (Fig. 8b), irrespectively of Ca content. This fact is assigned to the similar weak and medium basic sites concentration observed for all samples (Table 3), since these adsorption sites are those mainly related at this temperature range [50,51]. On the other hand, the

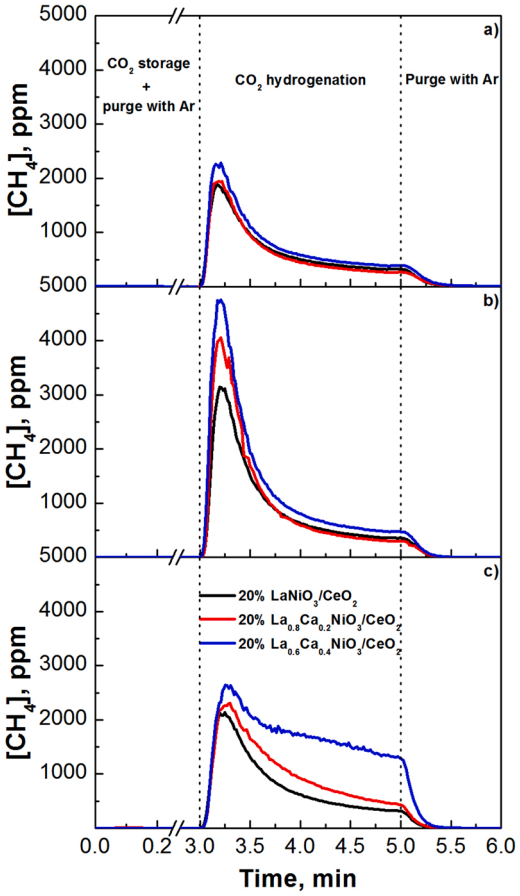

Fig. 8. CH_4 concentration profiles during a complete CO_2 adsorption and hydrogenation to CH_4 cycle at 280, 400 and 520 ºC for the DFMs obtained after the controlled reduction of: a) 20% $LaNiO_3/CeO_2$, b) 20% $La_{0.8}Ca_{0.2}NiO_3/CeO_2$ and c) 20% $La_{0.6}Ca_{0.4}NiO_3/CeO_2$ precursors.

maximum CH_4 production at 520 ºC (Fig. 8c) is observed at initial times for the non-substituted samples, whereas this process is delayed and takes place more progressively for the DFMs with increasing Ca contents. This fact is ascribed to the progressive increase in the concentration of the strong basic sites (Fig. 4 and Table 3), which are those mainly participating at high temperature due to their high stability [13,52,53]. Indeed, TPSR experiments (Fig. 5) revealed that increasing Ca contents favor the CO_2 methanation at higher temperatures (around 400 ºC) due the presence of carbonates linked to Ca-based species with higher stability. Thus, the best catalytic performance observed for the DFMs obtained from $La_{0.6}Ca_{0.4}NiO_3/CeO_2$ and $La_{0.5}Ca_{0.5}NiO_3/CeO_2$ precursors is ascribed to a better distribution of the different nature basic site. Ultimately, this aspect is related to a promoted distribution of CaO sites with respect to La_2O_3 ones, which leads to a promoted adsorbent utilization (Table 3). In summary, CH_4 production is favored as long as calcium content increases, especially at high temperatures.

3.2.3. *Evaluation of activity, stability and influence of the presence of O_2*

With the aim of evaluating the viability of the novel DFM obtained after the controlled reduction of 20% $La_{0.5}Ca_{0.5}NiO_3/CeO_2$ precursors its catalytic activity and stability has been compared with that of a conventional 15% Ni-15% CaO/Al_2O_3 formulation [12]. This study has been completed by evaluating the influence of the presence of O_2 during adsorption period on its CO_2 adsorption and hydrogenation efficiency.

Fig. 9 compares the carbon-based species (C-species) distribution for the 15% Ni-15% CaO/Al_2O_3 and 20% $La_{0.5}Ca_{0.5}NiO_3/CeO_2$-derived Dual Function Materials at 280, 360, 440 and 520 °C. As can be observed, the CH_4 production increases with higher reaction

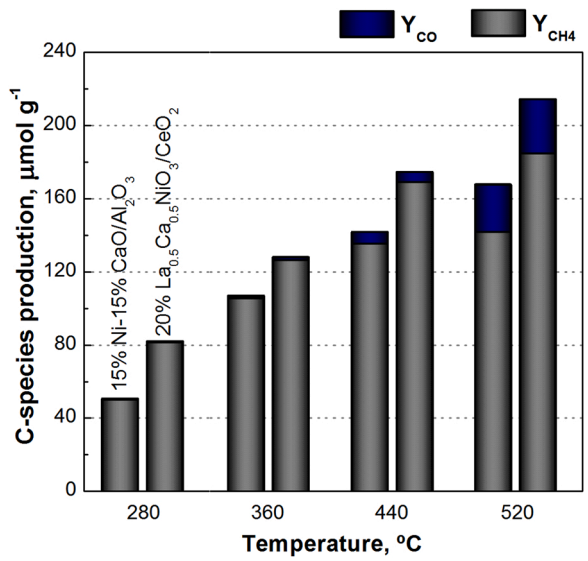

Fig. 9. C-species production for the conventional 15% Ni-15% CaO/Al_2O_3 20 (1st column) and the % $La_{0.5}Ca_{0.5}NiO_3/CeO_2$-derived (2nd column) DFMs at 4 different temperatures.

temperature for both DFMs, achieving these formulations their maximum CH_4 production at 520 ºC. The DFM obtained after the reduction of 20% $La_{0.5}Ca_{0.5}NiO_3/CeO_2$ presents higher CH_4 productions than conventional DFM (maximum of 188.8 vs. 143.0 µmol CH_4 g^{-1}) for all analyzed reaction temperatures. This fact is ascribed to a promoted distribution of CaO sites and lower particle size of Ni NPs with respect to conventional formulation due to the controlled ex-solution of these phases from the perovskite host. Note that adsorbent utilization values are 0.36 and 0.13, whereas Ni NPs average sizes of 4.4 and 17.8 nm are obtained for the 20% $La_{0.5}Ca_{0.5}NiO_3/CeO_2$-derived and 15% Ni-15% CaO/Al_2O_3 DFMs, respectively. Ultimately, these properties increase the proximity between storage (basic sites) and reducing (Ni^0) sites, promoting the transfer of dissociated H to hydrogenate near-adsorbed CO_2 [53]. Furthermore, the developed formulation presents higher selectivity towards CH_4 than conventional one, since CO production is lower throughout whole temperature range. In fact, the selectivity towards CH_4 is above 96% at optimum operation temperature, which discards a noticeable effect of the toxic CO. Thus, the novel 20% $La_{0.5}Ca_{0.5}NiO_3/CeO_2$ catalytic precursor can be considered as a promising base material for obtaining Dual Functioning Material with high efficiency for cyclic CO_2 adsorption/hydrogenation technology.

The stability and the adaptability of these DFMs have been evaluated by subjecting them to long-terms experiments under variable operational conditions (absence/presence of O_2 during adsorption period). Fig. 10 shows the evolution of CH_4 and CO productions with the number of CO_2 adsorption/hydrogenation cycle for the 15% Ni-15% CaO/Al_2O_3 and 20% $La_{0.5}Ca_{0.5}NiO_3/CeO_2$ samples at 480 ºC. As can be observed, the inclusion of oxygen during CO_2 adsorption period (cycle 11) negatively affects CH_4 production for both samples. In fact, CH_4 production drastically decreases between from 141 to 77 µmol CH_4 g^{-1} and from 188 to 89 µmol CH_4 g^{-1} for 15% Ni-15% CaO/Al_2O_3 and 20% $La_{0.5}Ca_{0.5}NiO_3/CeO_2$ samples, respectively. Zheng et al. [54] justified this point by the oxidation of the active metallic phase during the adsorption step. In agreement with their results, a small CO_2 signal is observed at the beginning of the hydrogenation period for the oxygen-containing experiment (Fig. S6). This fact reveals that some carbonates, adsorbed during the storage step, are released without being hydrogenated due to the absence of enough Ni^0 active sites to reduce them towards CH_4. As a result, a significant decrease in methane production is observed for the oxygen-containing experiment with respect to oxygen-free one. In contrast, CO production keeps almost constant for both samples, irrespectively the oxygen is present or absent in the feedstream during CO_2 adsorption period. This trend discards the promotion of RWGS reaction due to the partial oxidation of Ni^0 to NiO. Thus, a similar detrimental effect of oxygen can be noticed for here reported novel material with respect to conventional one, since CH_4 production decreases around 50% in both cases. However, it is worth to mention that the conventional catalyst (Fig. 10a) seems to be less stable since CH_4 production constantly decreases from cycle to cycle (cycle 11–20) under oxidizing conditions, whereas it remains constant for 20% $La_{0.5}Ca_{0.5}NiO_3/CeO_2$-derived DFM (Fig. 10b).

In order to gain insight on this aspect, the subsequent CO_2 adsorption/hydrogenation cycles (21−30) were again carried out in an oxygen-free environment. Both samples show a clear increase in CH_4 production just from the first cycle performed in the absence of oxygen (cycle 21). Specifically, the CH_4 production rises up to 109 and 164 µmol CH_4 g^{-1} for the 15% Ni-15% CaO/Al_2O_3 and 20% $La_{0.5}Ca_{0.5}NiO_3/CeO_2$ samples, respectively. Meanwhile, the CO production continues practically constant for both samples. Thus, these values represent an activity recovery of 77% and 88%, respectively. These results suggest that the novel DFM obtained after the controlled reduction of perovskite-based precursor present a higher capacity to restore activity under O_2 free environment during CO_2 adsorption. Note that this aspect is one of the main limitations for the widespread implementation of conventional Ni-based formulations [20,55,56]. This trend is ascribed to the high reducibility of different Ni species (Fig. 3), which ultimately promotes that Ni can be easily reduced back during the subsequent hydrogenation step that follows oxygen-free CO_2 adsorption period (cycle 21). Furthermore, the CH_4 production remains constant along the cycles carried out at each specific reaction conditions, which denotes a high stability during long-term experiments.

The stability of this novel DFM was analyzed in more detail by the characterization of the spent sample after long-term experiments. As can

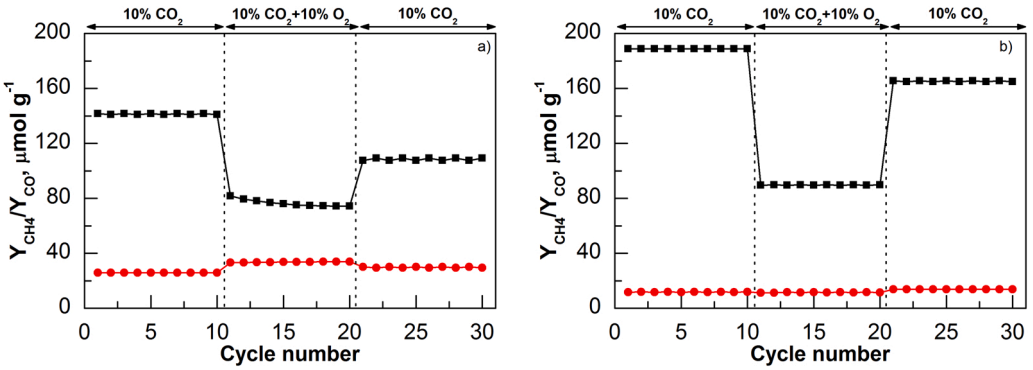

Fig. 10. CH_4 and CO productions at 480 ºC of: a) 15% Ni-15% CaO/Al_2O_3 and b) 20% $La_{0.5}Ca_{0.5}NiO_3/CeO_2$ samples with/without a 10% oxygen fed during the CO_2 adsorption step.

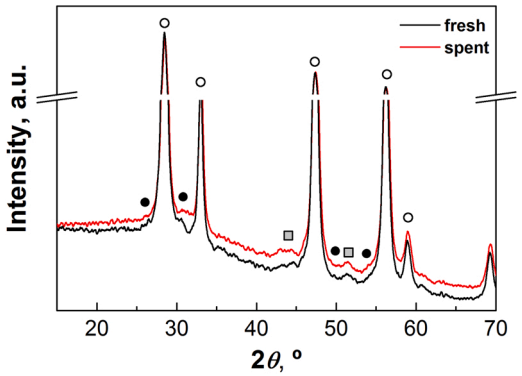

Fig. 11. XRD diffractograms of the spent 20% $La_{0.5}Ca_{0.5}NiO_3/CeO_2$-derived DFM before (fresh) and after (spent) stability test. (•) represents $La_2O_2CO_3$, (*) $La(OH)_3$, (fx1) Ni^0 and (○) CeO_2.

be observed, similar XRD diffractograms (Fig. 11) are obtained for the 20% $La_{0.5}Ca_{0.5}NiO_3/CeO_2$–derived sample before (fresh) and after (spent) stability test reported in Fig. 10. These results confirm the high stability of the crystalline phases identified for fresh sample and suggests that no noticeable agglomeration phenomenon occurs during repetitive cycles under different reaction conditions.

The later aspect is further confirmed by STEM-EDS images included in Fig. 12, where no significant changes have been identified in the different phases distribution and their morphology after stability test. As a result, quite similar textural properties as well as Ni NPs average size are obtained by N_2-adsorption-desorption experiments and STEM-EDS images (Table 6). Based on these results, the 20% $La_{0.5}Ca_{0.5}NiO_3/CeO_2$-derived DFM can be considered a superior candidate than conventional one (15% Ni-15% CaO/Al_2O_3) for CO_2 methanation under oxidizing conditions and long operation periods. However, the real-world applicability of these novel materials cannot be completely confirmed up to similar experiments in presence of 10–15% of steam, high N_2 concentrations and residual NO_x were performed. Furthermore, the catalytic behaviour after simulated hydrothermal aging should be evaluated. Currently, we are exploring this aspect, which would be the subject of future publications.

By last, considering the results reported in our previous works [57, 58], where we modeled, simulated and optimized the CO_2 adsorption and hydrogenation to CH_4, 60 s and 120 s are selected as the optimal adsorption and hydrogenation times, respectively. By the implementation of a valve system, these operating conditions enable to work with three identical beds in parallel, one operating in adsorption mode (post-combustion flue gas with diluted CO_2, 60 s) and two of them in regeneration mode (H_2, 120 s), producing methane with a high average formation rate. After 60 of operation, the former will be completely saturated and as consequence the feed stream will be changed to H_2. In order to maintain a continuous flow of the post-combustion flue gas with diluted CO_2, this feed stream will be deviated to 2nd bed, whereas the other one continues with hydrogenation in order to assess the complete regeneration of the DFM and to maximize CH_4 production. Finally, the cycle will be completed saturating the third bed and hydrogenating the other two beds. Thus, by this disposition of each the catalytic bed can operate under cycling CO_2 adsorption and hydrogenation modes and the post-combustion flue gas can be fed continuously to the system of three catalytic beds in parallel.

Based on the proposed configuration, these novel DFMs can be easily regenerated by subjecting them to longer hydrogenation periods (approximately 30 min) at relative high temperatures (above 400 °C). For that, it is necessary to dispose a fourth bed in parallel, as reserve. As a result, CO_2 and H_2 can be cyclically fed to three of the beds; meanwhile, the regeneration can be carried out on the deactivated bed, when it is necessary. This process can be carried out by subjecting the deactivated bed in each case to longer hydrogenation periods (i.e. 30 min) at high temperatures (above 400 °C), deviating the corresponding feed stream to the fourth reserve bed without interrupting the cycling operation in the other three beds.

Table 6
Specific surface areas (S_{BET}), pore volumes (V_p), average pore size (d_p) and Ni^0 average size (d_{Ni}) for the spent 20% $La_{0.5}Ca_{0.5}NiO_3/CeO_2$-derived DFM before and after stability test.

Sample	S_{BET}, $m^2\ g^{-1}$	V_p, $cm^3\ g^{-1}$	d_p, Á	d_{Ni}, nm[a]
20% $La_{0.5}Ca_{0.5}NiO_3/CeO_2$_fresh	29	0.13	152.9	6.1
20% $La_{0.5}Ca_{0.5}NiO_3/CeO_2$_spent	25	0.12	160.5	7.3

[a] Ni^0 average size Ni particle size distribution, estimated by measuring the size of, at least, 100 particles identified in STEM-EDS mappings.

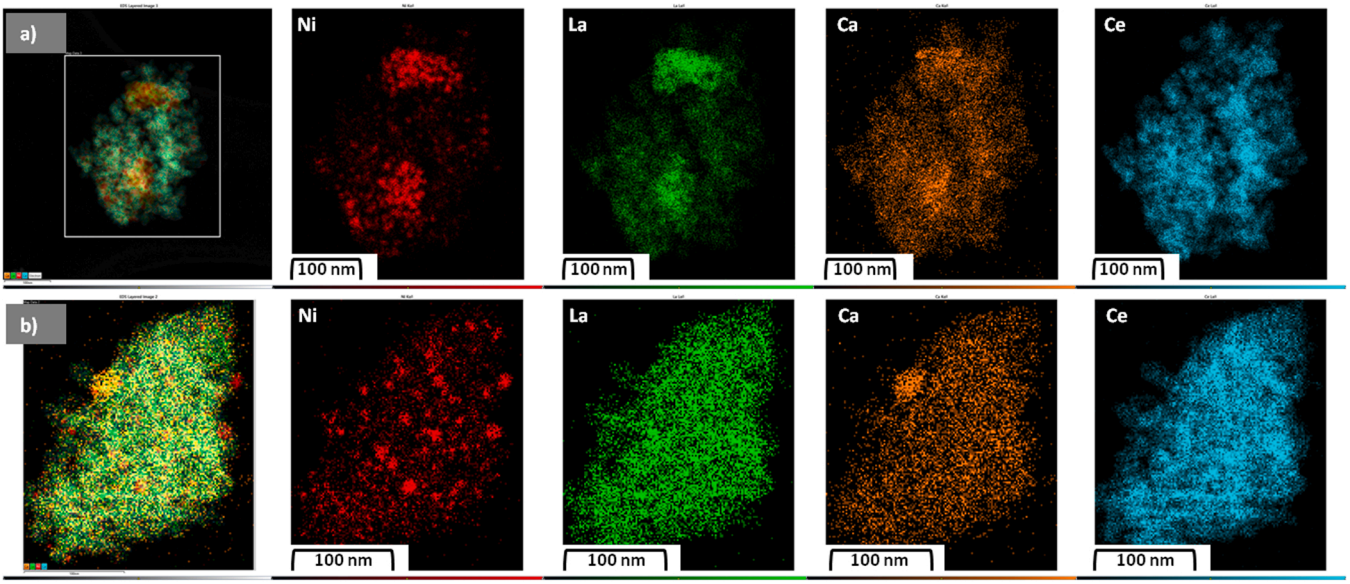

Fig. 12. STEM micrographs along with respective EDS elemental mapping of Ni, La, Ca and Ce for the spent 20% $La_{0.5}Ca_{0.5}NiO_3/CeO_2$-derived DFM: a) before and b) after stability test. The Ni particle sizes distribution was also included for each sample in form of histogram.

4. Conclusions

Novel dual function materials (DFMs) have been obtained after the controlled reduction of $La_{1-x}Ca_xNiO_3/CeO_2$-type precursors (with x = 0–0.5), synthesized by combined citric acid and wetness impregnation methods. The progressive insertion of Ca^{2+} substituting La^{3+} within the perovskite structure slightly promotes impurities formation (such as, La_2O_3, NiO or CaO) and progressively decreases specific surface area as well as samples reducibility. As a result, the corresponding dual function materials (DFMs), obtained after the controlled reduction of these precursors, also present variable physico-chemical properties. Specifically, the specific surface area decreases from 34 m^2 g^{-1} for $LaNiO_3/CeO_2$-derived DFM to 29 m^2 g^{-1} for $La_{0.5}Ca_{0.5}NiO_3/CeO_2$ one, which could be linked to the presence of higher amount of impurities in the corresponding perovskite-based precursor that could block the access to the pores. However, the highest influence of Ca doping is observed on surface basicity. As it is revealed by CO_2-TPD experiments, the progressive substitution of La^{3+} by Ca^{2+} leads a significant increase of surface basicity, especially that related to medium and strong basic sites. In agreement with STEM-EDX images, this fact is ascribed to an increasing accessibility of CO_2 adsorption sites as long as nanodispersed CaO is progressively substituting poorer distributed La_2O_3 sites formed after the perovskite destruction.

Among the prepared DFMs, $La_{0.5}Ca_{0.5}NiO_3/CeO_2$-derived one presents the maximum methane production capacity (188.8 μmol CH_4 g^{-1}), which is almost twice than that of the non-substituted sample (96.5 μmol CH_4 g^{-1}). The significant CH_4 production enhancement could be related with the fact that Ca can supply additional sites to adsorb CO_2 and as a consequence to active CO_2 methanation in a wider temperature range, as suggested by TPSR experiments. Furthermore, Ca seems to partially inhibit competitive adsorption of H_2O on CO_2 storage sites, which could further contribute to improving CO_2 adsorption.

The viability of $La_{0.5}Ca_{0.5}NiO_3/CeO_2$-derived DFM has been confirmed comparing its activity, selectivity, stability and adaptability with respect to that observed for the conventional 15% Ni-15% CaO/Al_2O_3 DFM. Interestingly, this novel formulation enhances the methane production (188.8 vs. 171.0 μmol CH_4 g^{-1}), the selectivity towards this compound (always above 88 vs. 85%) and the stability during long-term experiments under variable reaction conditions (absence/presence of O_2 during adsorption period). Taking into account that the later aspect is one of the main limitations of the conventional Ni-based formulations, here reported preliminary results open a new horizon in the possible real-world applicability of these novel materials.

CRediT authorship contribution statement

Jon A. Onrubia-Calvo: Conceptualization, Validation, Methodology, Investigation, Writing – original draft. **Beñat Pereda-Ayo:** Methodology, Visualization, Writing – review & editing. **Alejandro Bermejo-López:** Methodology, Visualization, Writing – review & editing. **José A. González-Marcos:** Methodology, Data curation, Supervision, Funding acquisition. **Juan R. González-Velasco:** Conceptualization, Supervision, Project administration, Funding acquisition.

Declaration of Competing Interest

The authors declare that they have no known competing financial interests or personal relationships that could have appeared to influence the work reported in this paper.

Acknowledgements

Support for this study was provided by Proyecto PID2019-105960RB-C21 by MCIN/AEI /10.13039/501100011033 and the Basque Government (Project IT1509-2022). One of the authors (JAOC) acknowledges the Post-doctoral Research Grant (DOCREC20/49) provided by the University of the Basque Country (UPV/EHU).

Appendix A. Supporting information

Supplementary data associated with this article can be found in the online version at doi:10.1016/j.apcatb.2022.122045.

References

[1] A. Modak, S. Jana, Advancement in porous adsorbents for post-combustion CO_2 capture, Microporous Mesoporous Mater. 276 (2019) 107–132.
[2] L. Zhang, Y. Liu, X. Li, L. Huang, D. Yu, X. Shi, H. Chen, S. Xing, Effects of soil map scales on simulating soil organic carbon changes of upland soils in Eastern China, Geoderma 312 (2018) 159–169.
[3] M. Jentsch, T. Trost, M. Sterner, Optimal use of power-to-gas energy storage systems in an 85% renewable energy scenario, Energy Procedia 46 (2014) 254–261.
[4] L. Schneider, E. Kötter, The geographic potential of power-to-gas in a german model region - trier-amprion 5, J. Energy Storage 1 (2015) 1–6.
[5] W. Li, H. Wang, X. Jiang, J. Zhu, Z. Liu, X. Guo, C. Song, A short review of recent advances in CO_2 hydrogenation to hydrocarbons over heterogeneous catalysts, RSC Adv. 8 (2018) 7651–7669.
[6] P. Sabatier, New Synthesis of Methane, Comptes Rendus., 134 (1902), pp. 514–516.
[7] O. Massol, S. Tchung-Ming, A. Banal-Estañol, Capturing industrial CO_2 emissions in Spain: infrastructures, costs and break-even prices, Energy Policy 115 (2018) 545–560.
[8] S. Budinis, S. Krevor, N.M. Dowell, N. Brandon, A. Hawkes, An assessment of CCS costs, barriers and potential, J. Energy Storage 22 (2018) 61–81.
[9] M.S. Duyar, M.A.A. Treviño, R.J. Farrauto, Dual function materials for CO_2 capture and conversion using renewable H_2, Appl. Catal. B Environm. 168–169 (2015) 370–376.
[10] Duyar M., Farrauto R., Park A. Methods systems and materials for capturing carbon dioxide and converting it to a chemical product (U.S Patent No. WO/2016/007825). University of Columbia: New York, NY, USA. 14–01-2016.
[11] S. Cimino, F. Boccia, L. Lisi, Effect of alkali promoters (Li, Na, K) on the performance of Ru/Al_2O_3 catalysts for CO_2 capture and hydrogenation to methane, J. CO_2 Util. 37 (2020) 195–203.
[12] A. Bermejo-López, B. Pereda-Ayo, J.A. González-Marcos, J.R. González-Velasco, Ni loading effects on dual function materials for capture and in-situ conversion of CO_2 to CH_4 using CaO or Na_2CO_3, J. CO_2 Util. 34 (2019) 576–587.
[13] A. Porta, R. Matarrese, C.G. Visconti, L. Castoldi, L. Lietti, Storage material effects on the performance of Ru-based CO_2 capture and methanation dual functioning materials, Ind. Eng. Chem. Res. 60 (2021) 6706–6718.
[14] Z. Zhou, N. Sun, B. Wang, Z. Han, S. Cao, D. Hu, T. Zhu, Q. Shen, W. Wei, 2D-Layered Ni–MgO–Al_2O_3 Nanosheets for Integrated Capture and Methanation of CO_2, ChemSusChem 13 (2020) 360–368.
[15] F. Kosaka, Y. Liu, S. Chen, T. Mochizuki, H. Takagi, A. Urakawa, K. Kuramoto, Enhanced activity of integrated CO_2 capture and reduction to CH_4 under pressurized conditions toward atmospheric CO_2 utilization, ACS Sustain. Chem. Eng. 9 (2021) 3452–3463.
[16] A. Bermejo-López, B. Pereda-Ayo, J.A. González-Marcos, J.R. González-Velasco, Mechanism of the CO_2 storage and in situ hydrogenation to CH_4. Temperature and adsorbent loading effects over Ru-CaO/Al_2O_3 and Ru-Na_2CO_3/Al_2O_3 catalysts, Appl. Catal. B-Environm. 256 (2019). Article 117845.
[17] S. Cimino, R. Russo, L. Lisi, Insights into the cyclic CO_2 capture and catalytic methanation over highly performing Li-Ru/Al_2O_3 dual function materials, Chem. Eng. J. (428) (2022). Article 131275.
[18] A. Bermejo-López, B. Pereda-Ayo, J.A. González-Marcos, J.R. González-Velasco, Alternate cycles of CO_2 storage and in situ hydrogenation to CH_4 on Ni–Na_2CO_3/Al_2O_3: influence of promoter addition and calcination temperature, Sustain. Energy Fuels 5 (2021) 1194–1210.
[19] M.S. Duyar, S. Wang, M.A. Arellano-Treviño, R.J. Farrauto, CO_2 utilization with a novel dual function material (DFM) for capture and catalytic conversion to synthetic natural gas: an, Update, J. CO_2 Util. 15 (2016) 65–71.
[20] M.A. Arellano-Treviño, Z. He, M.C. Libby, R.J. Farrauto, Catalysts and adsorbents for CO_2 capture and conversion with dual function materials: Limitations of Ni-containing DFMs for flue gas, J. CO_2 Util. 31 (2019) 143–151.
[21] A. Porta, C.G. Visconti, L. Castoldi, R. Matarrese, C. Jeong-Potter, R. Farrauto, L. Lietti, Ru-Ba synergistic effect in dual functioning materials for cyclic CO_2 capture and methanation, Appl. Catal. B Environ. 283 (2021). Article 119654.
[22] S. Wang, R.J. Farrauto, S. Karp, J.H. Jeon, E.T. Schrunk, Parametric, cyclic aging and characterization studies for CO_2 capture from flue gas and catalytic conversion to synthetic natural gas using a dual functional material (DFM), J. CO_2 Util. 27 (2018) 390–397.
[23] M.A.A. Aziz, A.A. Jalil, S. Triwahyono, A. Ahmad, CO_2 methanation over heterogeneous catalysts: recent progress and future prospects, Green. Chem. 17 (2015) 2647–2663.
[24] R. Ye, Q. Li, W. Gong, T. Wang, J.J. Razink, L. Lin, Y. Qin, Z. Zhou, H. Adidharma, J. Tang, A.G. Russell, M. Fan, Y. Yao, High-performance of nanostructured Ni/CeO_2 catalyst on CO_2 methanation, Appl. Catal. B Environ. 268 (2020). Article 118474.

[25] Y. Nishihata, J. Mizuki, T. Akao, H. Tanaka, M. Uenishi, M. Kimura, T. Okamoto, N. Hamada, Self-regeneration of a Pd-perovskite catalyst for automotive emissions control, Nature 418 (6894) (2002) 164–167.

[26] T. Maneerung, K. Hidajat, S. Kawi, K-doped $LaNiO_3$ perovskite for high-temperature water-gas shift of reformate gas: Role of potassium on suppressing methanation, Int. J. Hydrog.Energy 42 (2017) 9840–9857.

[27] J. Gao, L. Jia, W. Fang, Q. Li, H. Song, Methanation of carbon dioxide over the $LaNiO_3$ perovskite catalysts activated under the reactant stream, Fuel Chem. Technol. 37 (5) (2009) 573–577.

[28] T. Zhang, Q. Liu, Mesostructured cellular foam silica supported bimetallic $LaNi_{1-x}Co_xO_3$ catalyst for CO_2 methanation, Int. J. Hydrog. Energy 45 (2020) 4417–4426.

[29] J. Onrubia-Calvo, B. Pereda-Ayo, J.A. González-Marcos, A. Bueno-López, J. R. González-Velasco, Design of CeO_2-supported $LaNiO_3$ perovskites as precursors of highly active catalysts for CO_2 methanation, Catal. Sci. Technol. 11 (2021) 6065–6079.

[30] J.A. Onrubia-Calvo, A. Bermejo-López, S. Pérez-Vázquez, B. Pereda-Ayo, J. A. González-Marcos, J.R. González-Velasco, Applicability of $LaNiO_3$-derived catalysts as dual function materials for CO_2 capture and in-situ conversion to methane, Fuel 320 (2022). Article 123842.

[31] J.A. Onrubia, B. Pereda-Ayo, U. De-La-Torre, J.R. González-Velasco, Key factors in Sr-doped $LaBO_3$ (B=Co or Mn) perovskites for NO oxidation in efficient diesel exhaust purification, Appl. Catal. B Environ. 213 (2017) 198–210.

[32] J.A. Onrubia-Calvo, B. Pereda-Ayo, I. Cabrejas, U. De-La-Torre, J.R. González-Velasco, Ba-doped vs. Sr-doped $LaCoO_3$ perovskites as base catalyst in diesel exhaust purification, Mol. Catal. 488 (2020). Article 110913.

[33] Jon A. Onrubia-Calvo, Beñat Pereda-Ayo, Angel Caravaca, Unai De-La-Torre, Philippe Vernoux, Juan R. González-Velasco, Tailoring perovskite surface composition to design efficient lean NO_x trap Pd–$La_{1-x}A_xCoO_3/Al_2O_3$-type catalysts (with A = Sr or Ba), Appl. Catal. B-Environ. 266 (2020). Article 118628.

[34] J. Gallego, G. Sierra-Gallego, J. Tapia, F. Mondragón, C. Batiot-Dupeyrat, Activation of CO_2 on Ni/La_2O_3: non-isothermal kinetic study on the basis of thermogravimetric studies, React. Kinet. Mech. Catal. 119 (1) (2016) 179–193.

[35] B. Bakiz, F. Guinneton, M. Arab, A. Benlhachemi, S. Villain, P. Satre, J. Gavarri, Carbonatation and decarbonatation kinetics in the La_2O_3-$La_2O_2CO_3$ system under CO_2 gas flows, Adv. Mater. Sci. Eng. 2010 (2010) 1–6.

[36] Z. Boukha, A. Bermejo-López, B. Pereda-Ayo, J.A. González-Marcos, J.R. González-Velasco, Study on the promotional effect of lanthana addition on the performance of hydroxyapatite-supported Ni catalysts for the CO_2 methanation reaction, Appl. Catal. B Environ. 314 (2022), 121500.

[37] S.B. Jo, J.H. Woo, J.H. Lee, T.Y. Kim, H.I. Kang, S.C. Lee, J.C. Kim, CO_2 green technologies in CO_2 capture and direct utilization processes: methanation, reverse water-gas shift, and dry reforming of methane, Sustain, Energy Fuels 4 (2020) 5543–5549.

[38] Q. Liu, J. Gao, M. Zhang, H. Li, F. Gu, G. Xu, Z. Zhong, F. Su, Highly active and stable Ni/γ-Al_2O_3 catalysts selectively deposited with CeO_2 for CO methanation, RSC Adv. 4 (2014) 16094–16103.

[39] S. Singh, D. Zubenko, B.A. Rosen, Influence of $LaNiO_3$ shape on its solid-phase crystallization into coke-free reforming catalysts, ACS Catal. 6 (2016) 4199–4205.

[40] E. Yang, N.Y. Kim, G. Choi, S.S. Lim, D.J. Moon, Steam CO2 reforming of methane over La1-xCexNiO3 perovskite catalysts, 20th World Hydrogen Energy Conference, WHEC 2014, 3 (2014), pp. 1618–1626.

[41] J.Y. Do, N. Park, M.W. Seo, D. Lee, H. Ryu, M. Kang, Effective thermocatalytic carbon dioxide methanation on Ca-inserted $NiTiO_3$ perovskite, Fuel 271 (2020). Article 117624.

[42] I. Iglesias, A. Quindimil, F. Mariño, U. De-La-Torre, J.R. González-Velasco, Zr promotion effect in CO_2 methanation over ceria supported nickel catalysts, Int. J. Hydrog, Energy 44 (2019) 1710–1719.

[43] L. Atzori, M.G. Cutrufello, D. Meloni, R. Monaci, C. Cannas, D. Gazzoli, M.F. Sini, P. Deiana, E. Rombi, CO_2 methanation on hard-templated NiO-CeO_2 mixed oxides, Int. J. Hydrog. Energy 42 (2017) 20689–20702.

[44] S. Li, G. Liu, S. Zhang, K. An, Z. Ma, L. Wang, Y. Liu, Cerium-modified Ni-La_2O_3/ZrO_2 for CO_2 methanation, J. Energy Chem. 43 (2020) 155–164.

[45] R. Philipp, K. Fujimoto, FTIR spectroscopic study of carbon dioxide adsorption/desorption on magnesia/calcium oxide catalysts, J. Phys. Chem. 96 (1992) 9035–9038.

[46] H.S. Lim, G. Kim, Y. Kim, M. Lee, D. Kang, H. Lee, J.W. Lee, Ni-exsolved $La_{1-x}Ca_xNiO_3$ perovskites for improving CO_2 methanation, Chem. Eng. J. 412 (2021). Article 127557.

[47] B. Dou, C. Wang, Y. Song, H. Chen, B. Jiang, M. Yang, Y. Xu, Solid sorbents for in-situ CO_2 removal during sorption-enhanced steam reforming process: A review, Renew. Sust. Energy Rev. 53 (2016) 536–546.

[48] M. Shokrollahi Yancheshmeh, H.R. Radfarnia, M.C. Iliuta, High temperature CO_2 sorbents and their application for hydrogen production by sorption enhanced steam reforming process, Chem. Eng. J. 283 (2016) 420–444.

[49] Y. Yu, Z. Bian, F. Song, J. Wang, Q. Zhong, S. Kawi, Influence of calcination temperature on activity and selectivity of Ni–CeO_2 and Ni–$Ce_{0.8}Zr_{0.2}O_2$ catalysts for CO_2 methanation top, Catal 61 (2018) 1514–1527.

[50] A. Al-Mamoori, H. Thakkar, X. Li, A.A. Rownaghi, F. Rezaei, Development of potassium- and sodium-promoted CaO adsorbents for CO_2 capture at high temperatures, Ind. Eng. Chem. Res. 56 (2017) 8292–8300.

[51] C.H. Lee, S.W. Choi, H.J. Yoon, H.J. Kwon, H.C. Lee, S.G. Jeon, K.B. Lee, Na_2CO_3-doped CaO-based high-temperature CO_2 sorbent and its sorption kinetics, Chem. Eng. J. 352 (2018) 103–109.

[52] J. Ashok, Y. Kathiraser, M.L. Ang, S. Kawi, Bi-functional hydrotalcite-derived NiO–CaO–Al_2O_3 catalysts for steam reforming of biomass and/or tar model compound at low steam-to-carbon conditions, Appl. Catal. B-Environ., 172- 173 (2015) 116–128.

[53] A. Bermejo-López, B. Pereda-Ayo, J.A. Onrubia-Calvo, J.A. González-Marcos, J. R. González-Velasco, Tuning basicity of dual function materials widens operation temperature window for efficient CO_2 adsorption and hydrogenation to CH_4, J. CO_2 Util. 58 (2022). Article 101922.

[54] Q. Zheng, R. Farrauto, A. Chau Nguyen, Adsorption and methanation of Flue Gas CO_2 with dual functional catalytic materials: a parametric study, Ind. Eng. Chem. Res. 55 (2016) 6768–6776.

[55] B. Mutz, H.W.P. Carvalho, S. Mangold, W. Kleist, J. Grunwaldt, Methanation of CO_2: structural response of a Ni-based catalyst under fluctuating reaction conditions unraveled by operando spectroscopy, J. Catal. 327 (2015) 48–53.

[56] B. Mutz, A.M. Gänzler, M. Nachtegaal, O. Müller, R. Frahm, W. Kleist, J. Grunwaldt, Surface oxidation of supported ni particles and its impact on the catalytic performance during dynamically operated methanation of CO_2, Catalysts 7 (2017).

[57] A. Bermejo-López, B. Pereda-Ayo, J.A. González-Marcos, J.R. González-Velasco, Simulation-based optimization of cycle timing for CO_2 capture and hydrogenation with dual function catalyst, Catal. Today 394- 396 (2022) 314–324.

[58] A. Bermejo-López, B. Pereda-Ayo, J.A. González-Marcos, J.R. González-Velasco, Modeling the CO_2 capture and in situ conversion to CH_4 on dual function Ru-Na_2CO_3/Al2O_3, Catal., J. CO_2 Util. 42 (2020), 101351.